Doppler-Resilient Orthogonal Signal-Division Multiplexing for Underwater Acoustic Communication

Tadashi Ebihara, *Member, IEEE*, and Geert Leus, *Fellow, IEEE*

Abstract—Underwater acoustic (UWA) channels are characterized by a severe spread in time and frequency, and are usually labeled as "doubly spread channels." In this paper, we propose Doppler-resilient orthogonal signal-division multiplexing (D–OSDM), to provide a highly reliable communication environment in doubly spread channels for UWA communication. D–OSDM multiplexes several data vectors in addition to a pilot vector, and preserves orthogonality among them even after propagation through doubly spread channels, under the assumption that the channel can be modeled by a basis expansion model (BEM). We describe the signal processing steps at the transmitter and the receiver for D–OSDM, and evaluate its performance by both simulations and experiments. To generate a doubly spread channel, a test tank with a wave generator is employed. The obtained results suggest that D–OSDM can provide low-power and high-quality UWA communications in channels with large delay and Doppler spreads; for example, D–OSDM succeeds to achieve a block error rate (BLER) of 10^{-3} while BEM-based orthogonal frequency-division multiplexing (OFDM) has a BLER floor of 10^{-2} in the experiments. Equivalently, D–OSDM can reduce the signal power required for communications to achieve the same BER significantly. Overall, it was found that D–OSDM can become a powerful communication tool for underwater operations.

Index Terms—Doppler, multipath channels, underwater acoustic (UWA) communication.

I. Introduction

UNDERWATER ACOUSTIC (UWA) communication enables a wireless link in an underwater environment by the transmission of acoustic waves, and provides flexible wide area communication in an underwater environment. Recently, UWA communication has become an essential necessity for underwater operations, such as oceanographic observation and offshore development, and the scope of its application is still growing. For example, oceanographic observation systems utilize UWA communication to establish a point-to-point data link (e.g., from a sensor on the seafloor to a buoy on the sea surface). However, new underwater projects become more complicated. For instance, to monitor the dynamic behavior of the ocean environment, multipoint measurements are gathered and UWA communication is adopted to establish a complicated communication network between the sensors (e.g., there are a number of sensors on the seafloor and underwater vehicles act as hubs of the underwater network [1]–[6]). As a result, UWA communication makes a significant contribution to the development of underwater applications. Moreover, the communication quality, reliability, and speed of UWA communication are important factors to determine the performance of the application. As a result, the design of the physical layer is an important issue, as well as the development of the network layer.

From the viewpoint of physical layer design, the UWA channel is a challenging environment to provide a reliable link. UWA channels, especially shallow-water ducts, are characterized by a severe spread in time and frequency. Induced by severe multipath propagation, the channel suffers from a large delay spread giving rise to intersymbol interference (ISI). Moreover, the motion of the communication platform and the sea surface generates a Doppler shift for every propagation path, generally resulting in a large Doppler spread. This ISI and Doppler spread can cause errors and affect the communication quality. Because the signal bandwidth is much larger than the inverse delay spread, and the sound speed in underwater is far smaller than the light speed used in radio, the effect of the ISI and Doppler spread in UWA communication can become several orders of magnitude greater than the one in radio communication, hence, these phenomena serve as a barrier to UWA communication.

As a result, communication systems based on two major modulation techniques, single-carrier and multicarrier modulation, have actively been researched to cope with delay and Doppler spread. For single-carrier communication, the use of an adaptive equalizer [e.g., a decision feedback equalizer with a recursive least squares algorithm (RLS–DFE)] has been found effective to cope with the ISI [7], [8], and a channel tracker can counteract the large Doppler spread [9], [10]. The use of error correction coding, such as Turbo coding, has also been demonstrated to improve the communication quality [11]. For multicarrier communication, orthogonal frequency-division multiplexing (OFDM) has attracted a lot of attention due to the low

receiver complexity [12], where a Doppler shift correction has been found useful to cope with the Doppler spread [13], [14], assuming that all propagation paths have the same frequency shift. Moreover, large Doppler spreads can be handled by a basis expansion model (BEM)-based signal design and the use of Turbo coding [15]–[20].

On the other hand, we have focused on another scheme for UWA communication: orthogonal signal-division multiplexing (OSDM) [21]–[23]. OSDM is a block transmission technique for a single user; it multiplexes several data vectors—a pilot signal as well as messages—into a single data stream and provides reliable channel sensing. The basic signal structure is compatible with the chip-interleaved block spread code-division multiple-access (CIBS–CDMA) system [25]. We found that OSDM with a multichannel receiver is attractive for UWA communication in terms of communication quality; in a static channel and for a realistic complexity, it achieves a far better bit error rate (BER) performance compared to other schemes, such as a single-carrier system based on RLS–DFE or a multicarrier system based on OFDM [26]. However, the performance of OSDM drops in a dynamic channel due to the Doppler spread, and it is highly desirable if we can suppress such a performance degradation in doubly spread channels.

In wireless mobile systems, the idea of orthogonal multiple access has been proposed [27]. Orthogonal multiple access is a block transmission technique for multiple users and its basic signal structure is an adaptation of CIBS–CDMA. This technique preserves mutual orthogonality among the users, even after propagation through doubly spread channels under the assumption that the channel can be modeled by a BEM. However, this method requires perfect channel information at the receiver, prior to receiver processing.

In this paper, we propose Doppler-resilient OSDM (D–OSDM), to provide a viable alternative offering a highly reliable communication environment for UWA communication under delay and Doppler spread. D–OSDM is a combination of the OSDM technique and orthogonal multiple access which are perfectly complementary; orthogonal multiple access provides OSDM the robustness to Doppler spread, while OSDM provides orthogonal multiple access accurate channel sensing. Moreover, we also propose a D–OSDM receiver with frequency-domain oversampling, based on the idea presented in [19]. We design D–OSDM to utilize the full energy spread in the frequency domain if the channel is modeled as a BEM, and evaluate its performance by both simulations and test-tank experiments. Section II introduces the D–OSDM scheme following an overview of the BEM channel model. Sections III and IV evaluate the performance of D–OSDM by simulations and experiments. Section V presents our conclusions.

Notation: We use upper/lower bold face letters to denote matrices/row vectors, and define $\boldsymbol{x}[i]$ as the ith element of the vector $\boldsymbol{x}$ starting with index 0. $(\cdot)^*$ and $(\cdot)^{\mathrm{T}}$ denote conjugate transpose and transpose, respectively. Positive real numbers, integer numbers, and positive integer numbers are defined as $\mathbb{R}^+$, $\mathbb{Z}$, and $\mathbb{Z}^+$, respectively. $\boldsymbol{0}_{R \times C}$, $\boldsymbol{F}_N$, and $\boldsymbol{I}_M$ represent the $R \times C$ all-zero matrix, the $N \times N$ inverse discrete Fourier transform (IDFT) matrix, and the $M \times M$ identity matrix, respectively. W_{MN}^k represents an element of the IDFT matrix,

where $W_{MN}^k = \exp[2\pi\sqrt{-1}k/(MN)]$ and $k \in \mathbb{Z}$. $\boldsymbol{Z}_N$ represents a cyclic shift matrix of size $N \times N$, and

$$\boldsymbol{Z}_N = \begin{pmatrix} 0 & 1 & 0 & \cdots & 0 & 0 \\ 0 & 0 & 1 & \cdots & 0 & 0 \\ \vdots & \vdots & \vdots & \ddots & \vdots & \vdots \\ 0 & 0 & 0 & \cdots & 0 & 1 \\ 1 & 0 & 0 & \cdots & 0 & 0 \end{pmatrix}.$$

II. DOPPLER-RESILIENT OSDM

A. Communication in Doubly Spread BEM Channels

At first, we review communication over doubly spread channels that can be modeled by a BEM. We consider a block data transmission using a discrete-time baseband model. Suppose a transmission message is modeled by the complex-valued $1 \times MN$ vector $\boldsymbol{x}$, where $M \in \mathbb{Z}^+$ and $N \in \mathbb{Z}^+$. A transmitter pads $L \in \mathbb{Z}^+$ zeros to the tail of this message [called zero-padding (ZP)] and transmits it over the channel with rate $1/T \in \mathbb{R}^+$, where it will be distorted by a delay and Doppler spread. We assume that the received signal can be represented by a linear combination of delay- and Doppler-shifted copies of the transmitted signal. More specifically, we will adopt a BEM [27], [28] with maximum (discrete) delay spread and maximum (discrete) Doppler shift bounded by L and $Q \in \mathbb{Z}^+$, respectively. In this case, the received sequence at sampling rate $1/T$, represented by the $1 \times (MN + L - 1)$ vector $\boldsymbol{y}$, can be represented as

$$\boldsymbol{y} = \boldsymbol{x} \sum_{q=-Q}^{Q} \boldsymbol{H}_q \boldsymbol{\Lambda}_q + \boldsymbol{\eta} \qquad (1)$$

where $\boldsymbol{\eta}$ is the additive noise. In (1), the $MN \times (MN + L - 1)$ matrix $\boldsymbol{H}_q$ and the $(MN + L - 1) \times (MN + L - 1)$ matrix $\boldsymbol{\Lambda}_q$, respectively, describe the effects of the delay and Doppler shifts. In detail, we can write

$$\boldsymbol{H}_q = \begin{pmatrix} h_{0,q} & h_{1,q} & \cdots & h_{L-1,q} & 0 & \cdots & 0 \\ 0 & h_{0,q} & \cdots & h_{L-2,q} & h_{L-1,q} & \cdots & 0 \\ \vdots & \vdots & \ddots & \vdots & \vdots & \ddots & \vdots \\ 0 & 0 & \cdot & h_{0,q} & h_{1,q} & \cdots & h_{L-1,q} \end{pmatrix}$$
$$(2)$$
$$\boldsymbol{\Lambda}_q = \mathrm{diag}\left(W_{MN}^0, W_{MN}^q, \ldots, W_{MN}^{(MN+L-2)q} \right) \qquad (3)$$

where $h_{l,q}$ represents the channel impulse response at Doppler scale q, and $h_{l,q} = 0$ for $l < 0$ and $l \geq L$. The diagonal components of $\boldsymbol{\Lambda}_q$ introduce a Doppler shift of $q/(MNT)$, where $T \in \mathbb{R}^+$ is the time-domain resolution. Note that there is only a small difference between BEM and real channels; the Doppler shifts are discretized in a BEM channel, whereas most real Doppler spread channels have a continuous Doppler spectrum. However, such a BEM modeling error can be kept very small in most practical situations [29]. Moreover, our experiments and simulations show that D–OSDM, whose design is based on a BEM channel, achieves a good communication quality even in real Doppler spread channels as well as in simulated channels with a continuous Doppler spectrum.

The scope of our study is to provide a new communication technique by estimating $h_{l,q}(l = 0, 1, \ldots, M - 1$ and $q = -Q, -Q + 1, \ldots, Q)$ and performing equalization. Note that although the channel length is limited to L, we will always
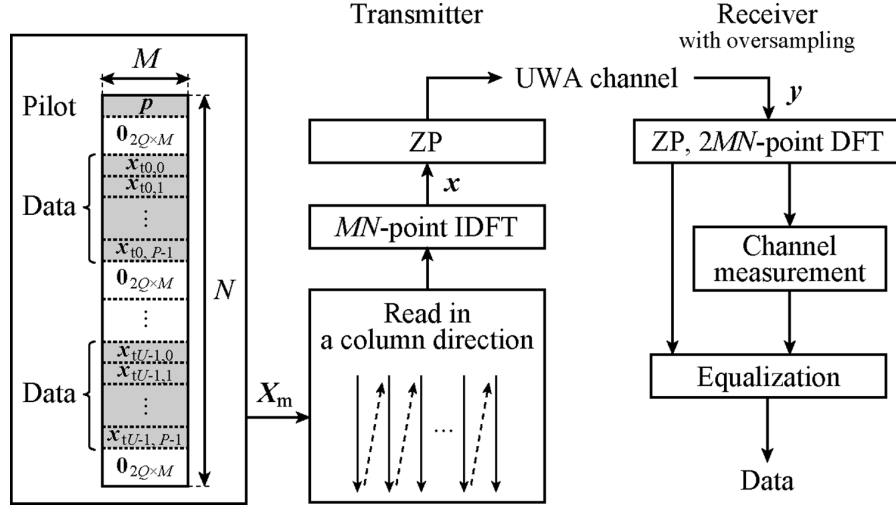
Fig. 1. Block diagram of D–OFDM at the transmitter and the receiver.

TABLE I
PARAMETERS USED FOR THE DESIGN OF D–OFDM AND D–OSDM

Message length		M
Total number of messages per group		P
Total number of groups		U
Maximum Doppler shift		Q
Maximum delay spread		L
Block length		$MN + L$
Spectral efficiency (bit/s/Hz)		$bc_{\mathrm{rate}}MPU/(MN + L)$
Receiver complexity	D-OSDM without frequency-domain oversampling	$\mathcal{O}\left(M^3\right)$
	D-OSDM with frequency-domain oversampling	$\mathcal{O}\left(M^3\right)$
	D-OFDM with frequency-domain oversampling	$\mathcal{O}\left(M\right)$

* $N = (1 + 2Q) + U(P + 2Q)$, b is the number of bits per symbol, and c_{rate} is the code rate.

estimate $M \geq L$ time-varying channel taps. Therefore, we focus on nonsparse channel estimation [e.g., using least squares (LS)] in our paper. In the following section, we first review the BEM-based OFDM scheme of [19], and call this Doppler-resilient OFDM (D–OFDM) in this paper. Then, we introduce our D–OSDM design at the transmitter and the receiver, also adopting doubly spread BEM channels.

B. Review of D–OFDM

Fig. 1 shows a block diagram of the D–OFDM operations. Table I shows the parameters used for the design of D–OFDM, where Q and L are determined based on the physical channel environment. First, let us consider the data matrix

$$\boldsymbol{X}_{\mathrm{m}} = \left(\boldsymbol{p}^{\mathrm{T}}, \boldsymbol{0}_{2Q \times M}^{\mathrm{T}}, \boldsymbol{x}_{\mathrm{t}0,0}^{\mathrm{T}}, \boldsymbol{x}_{\mathrm{t}0,1}^{\mathrm{T}}, \ldots, \right.$$
$$\boldsymbol{x}_{\mathrm{t}0,P-1}^{\mathrm{T}}, \boldsymbol{0}_{2Q \times M}^{\mathrm{T}}, \boldsymbol{x}_{\mathrm{t}1,0}^{\mathrm{T}}, \boldsymbol{x}_{\mathrm{t}1,1}^{\mathrm{T}}, \ldots,$$
$$\boldsymbol{x}_{\mathrm{t}1,P-1}^{\mathrm{T}}, \boldsymbol{0}_{2Q \times M}^{\mathrm{T}}, \ldots, \boldsymbol{0}_{2Q \times M}^{\mathrm{T}}, \boldsymbol{x}_{\mathrm{t}U-1,0}^{\mathrm{T}},$$
$$\left. \boldsymbol{x}_{\mathrm{t}U-1,1}^{\mathrm{T}}, \ldots, \boldsymbol{x}_{\mathrm{t}U-1,P-1}^{\mathrm{T}}, \boldsymbol{0}_{2Q \times M}^{\mathrm{T}} \right)^{\mathrm{T}} \quad (4)$$

where $\boldsymbol{p}$ is a pilot vector of length M and $\boldsymbol{x}_{\mathrm{t}u,p}$ is the transmission message ($u = 0, 1, \ldots, U - 1$ and $p = 0, 1, \ldots, P - 1$, with $P \in \mathbb{Z}^+$ and $U \in \mathbb{Z}^+$). Note that $N = (1 + 2Q) + U(P + 2Q)$. Each $\boldsymbol{x}_{\mathrm{t}u,p}$ contains a different message whose elements

are modulated symbols [e.g., by quadrature phase-shift keying (QPSK)] expressed as complex numbers.

The transmitter calculates the transmitted block signal $\boldsymbol{x}$ by reading $\boldsymbol{X}_{\mathrm{m}}$ columnwise and applying the MN-point IDFT matrix, and finally it pads L zeros to $\boldsymbol{x}$, as shown in Fig. 1. Fig. 2 shows the structure of a D–OFDM block (sample rate $1/T$) in the time–frequency domain, when $M = 2, P = 2, U = 2$, and $Q = 1$ ($N = 11$). As shown in the figure, there are MN subcarriers, M comb-type pilot subcarriers, MU groups of P data subcarriers, and the remaining subcarriers are null subcarriers on either side of the pilot subcarriers and data subcarrier groups. Although the data subcarriers are facing intercarrier interference (ICI) in Doppler spread channels, the receiver can measure the channel impulse responses under Doppler shift from the pilot subcarriers and null subcarriers on either side of the pilots. As such, it can obtain the transmitted message by channel equalization. From Fig. 2, it is also clear that the quadruple (M, P, U, Q) determines the block length and the spectral efficiency. The block length and the spectral efficiency of D–OFDM are also shown in Table I.

The receiver pads zeros to the received sequence $\boldsymbol{y}$ to turn it into a vector of length $2MN$ and applies the $2MN$-point DFT matrix (frequency-domain oversampling with an oversampling factor of 2). In the equalization process, the receiver obtains P
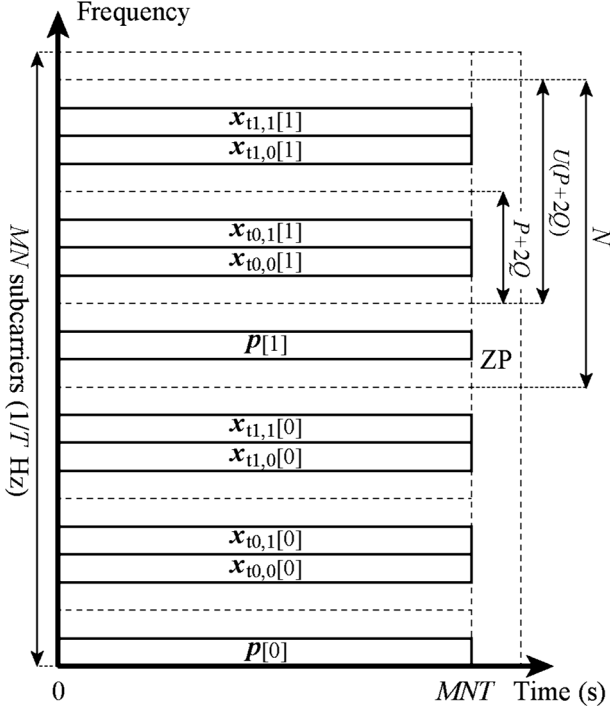
Fig. 2. Structure of the transmitted signal (D–OFDM) in the time–frequency domain, when $M = 2, P = 2, U = 2$, and $Q = 1$.

message symbols from $2P + 4Q - 1$ oversampled subcarriers (they correspond to $P + 2Q$ subcarriers in Fig. 2). When the receiver employs K hydrophones, the receiver obtains P message symbols from $K(2P + 4Q - 1)$ oversampled subcarriers by using LS for all MU groups. In this case, the total complexity of D–OFDM with frequency-domain oversampling becomes $\mathcal{O}(M)$.[1]

C. D–OSDM Operation at the Transmitter

Fig. 3 shows a block diagram of the D–OSDM operations. Table I again shows the parameters used for the design of D–OSDM. The transmitter calculates the transmitted block signal $\boldsymbol{x}$ by reading $\boldsymbol{X}_{\mathrm{m}}$ row-wise and applying a specific transformation matrix, and finally it pads L zeros to $\boldsymbol{x}$, as shown

---

[1]We assume that we obtain $\boldsymbol{a}$ from $\boldsymbol{b} = \boldsymbol{a}\boldsymbol{C}$ using LS, where $\boldsymbol{a}, \boldsymbol{b}$, and $\boldsymbol{C}$ are a vector of length α, a vector of length β, and a matrix of size $\alpha \times \beta$, respectively. In this case, the complexity (the number of multiplications) of computing $\boldsymbol{C}\boldsymbol{C}^*$ and $(\boldsymbol{C}\boldsymbol{C}^*)^{-1}$ becomes $\mathcal{O}(\alpha^2\beta)$ and $\mathcal{O}(\alpha^3)$, respectively. Since $\alpha < \beta$, the total complexity to calculate $\boldsymbol{a} = \boldsymbol{b}\boldsymbol{C}^*(\boldsymbol{C}\boldsymbol{C}^*)^{-1}$ is $\mathcal{O}(\alpha^2\beta)$. Hence, the complexity to obtain P message symbols from $K(2P + 4Q - 1)$ oversampled subcarriers by using LS becomes $\mathcal{O}(P^3)$. However, since $M \gg P$, the total complexity (calculating LS for all MU groups) becomes $\mathcal{O}(M)$.

in Fig. 3. In more detail, the transmitter reads $\boldsymbol{X}_{\mathrm{m}}$ row-wise resulting in a vector of length MN, given by

$$\boldsymbol{x}_{\mathrm{m}} = (\boldsymbol{p}, \boldsymbol{0}_{1 \times 2QM}, \boldsymbol{x}_{\mathrm{t}0}, \boldsymbol{0}_{1 \times 2QM}, \boldsymbol{x}_{\mathrm{t}1}, \boldsymbol{0}_{1 \times 2QM}, \dots,$$
$$\boldsymbol{0}_{1 \times 2QM}, \boldsymbol{x}_{\mathrm{t}U-1}, \boldsymbol{0}_{1 \times 2QM}) \quad (5)$$

where $\boldsymbol{x}_{\mathrm{t}u}$ is a group of messages

$$\boldsymbol{x}_{\mathrm{t}u} = (\boldsymbol{x}_{\mathrm{t}u,0}, \boldsymbol{x}_{\mathrm{t}u,1}, \dots, \boldsymbol{x}_{\mathrm{t}u,P-1})$$

and as before

$$N = (1 + 2Q) + U(P + 2Q).$$

Then, the transmitter applies the transformation matrix $\boldsymbol{F}_N \otimes \boldsymbol{I}_M$ to $\boldsymbol{x}_{\mathrm{m}}$, and obtains a single transmitted data stream of length MN, $\boldsymbol{x}$, according to

$$\boldsymbol{x} = \boldsymbol{x}_{\mathrm{m}}(\boldsymbol{F}_N \otimes \boldsymbol{I}_M). \quad (6)$$

By applying the transformation matrix, each element of $\boldsymbol{p}$ and $\boldsymbol{x}_{\mathrm{t}u}$ appears periodically in both the time and frequency domains with appropriate guard bands. Finally, the transmitter performs ZP of length L to $\boldsymbol{x}$, and the zero-padded sequence is transmitted over the channel.

To better understand what kind of signals are transmitted over the channel, we investigate $\boldsymbol{x}$ in the time–frequency domain. If we calculate $\boldsymbol{x}$ using (6), it is clear that every symbol (element of $\boldsymbol{p}$ and $\boldsymbol{x}_{\mathrm{t}u,p}$) is modulated by a Dirac train (each element of the train corresponds to a specific row of the IDFT matrix) with N pulses separated in time by M samples. If we calculate the spectrum (DFT transform) of $\boldsymbol{x}$, the output becomes (7), shown at the bottom of the page, where $\boldsymbol{f}_r = (W_{MN}^0, W_{MN}^{-r}, \dots, W_{MN}^{-(M-1)r})$. Expression (7) shows that every symbol also appears as a Dirac train in the frequency domain, but now with M pulses separated in frequency by N samples. This way, D–OSDM fully exploits the time–frequency diversity of the channel. In D–OSDM, the pilot and data vectors are repeated in both time and frequency and every symbol is modulated on a waveform that occupies an $M \times N$ lattice in the time–frequency domain.

Fig. 4 shows the structure of $\boldsymbol{x}$ in the time–frequency domain, when $M = 2, P = 2, U = 2$, and $Q = 1$ ($N = 11$). As shown in the figure, there are MN subcarriers in the frequency domain; M pilot subcarriers and U groups of P data subcarriers periodically appear M times in the spectrum of $\boldsymbol{x}$. By inserting zero vectors in between the vectors $\boldsymbol{x}_{\mathrm{t}u}$ in the precoding process [see (5)], there are Q null subcarriers (guard bands) on either side of the pilot subcarriers and data subcarrier groups. Note

$$\boldsymbol{x}\boldsymbol{F}_{MN}^* = \boldsymbol{x}_{\mathrm{m}}(\boldsymbol{F}_N \otimes \boldsymbol{I}_M)\boldsymbol{F}_{MN}^*$$

$$= \boldsymbol{x}_{\mathrm{m}}\begin{pmatrix} \boldsymbol{f}_0^{\mathrm{T}} & \boldsymbol{0}_{M \times 1} & \cdots & \boldsymbol{0}_{M \times 1} & \boldsymbol{f}_N^{\mathrm{T}} & \cdots & \boldsymbol{0}_{M \times 1} & \boldsymbol{f}_{(M-1)N}^{\mathrm{T}} & \boldsymbol{0}_{M \times 1} & \cdots & \boldsymbol{0}_{M \times 1} \\ \boldsymbol{0}_{M \times 1} & \boldsymbol{f}_1^{\mathrm{T}} & \cdots & \boldsymbol{0}_{M \times 1} & \boldsymbol{0}_{M \times 1} & \cdots & \boldsymbol{0}_{M \times 1} & \boldsymbol{0}_{M \times 1} & \boldsymbol{f}_{(M-1)N+1}^{\mathrm{T}} & \cdots & \boldsymbol{0}_{M \times 1} \\ \vdots & \vdots & \ddots & \vdots & \vdots & \ddots & \vdots & \vdots & \vdots & \ddots & \vdots \\ \boldsymbol{0}_{M \times 1} & \boldsymbol{0}_{M \times 1} & \cdots & \boldsymbol{f}_{N-1}^{\mathrm{T}} & \boldsymbol{0}_{M \times 1} & \cdots & \boldsymbol{f}_{(M-1)N-1}^{\mathrm{T}} & \boldsymbol{0}_{M \times 1} & \boldsymbol{0}_{M \times 1} & \cdots & \boldsymbol{f}_{MN-1}^{\mathrm{T}} \end{pmatrix} \quad (7)$$
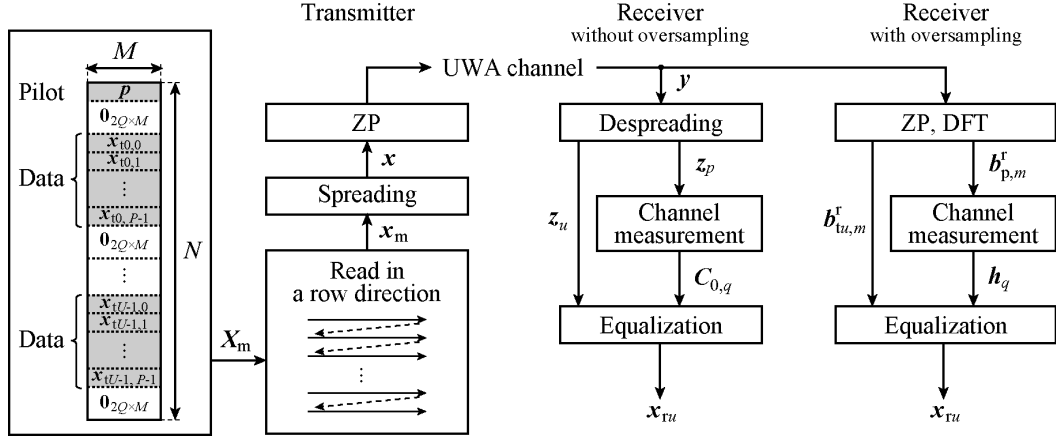
Fig. 3.	Block diagram of D–OSDM at the transmitter and the receiver.

that D–OSDM for $P = 1$ and $Q = 0$ corresponds to the existing OSDM [26]. From Fig. 4, it is also clear that the quadruple (M, P, U, Q) determines the block length and the spectral efficiency, as for D–OFDM. We can increase the spectral efficiency (effective data rate) by increasing both P and U, in exchange for communication quality, but an increase of P is more effective than the one of U as we will illustrate in Section III-B.

If we apply a doubly spread BEM channel on $\boldsymbol{x}_{\mathrm{m}}$, the different groups ($\boldsymbol{p}$ and $\boldsymbol{x}_{tu}$) do not overlap in both time and frequency domains, if the maximum delay and Doppler spread are bounded by L (remember that $M \geq L$) and Q, respectively. This is because we employ ZP and null subcarriers. Focusing on a specific group (e.g., $\boldsymbol{x}_{tu}$), a set of lattices corresponding to that specific group do overlap in time and frequency, under doubly spread BEM channels. However, the mutual orthogonality among those groups of latices is still preserved at the receiver due to the orthogonality of the rows of the IDFT matrix. Note that this is in contrast to [16].

D. D–OSDM Operation at the Receiver

As mentioned, to develop our D–OSDM scheme, we represent the effect of UWA channel spread in time and frequency using a BEM. The receiver obtains an estimate of every transmitted message $\boldsymbol{x}_{tu,p}$ by applying a transformation matrix and performing channel equalization, as shown in Fig. 3. The received data stream $\boldsymbol{y}$ can be expressed as in (1). The receiver then applies the transformation matrix $\boldsymbol{A}(\boldsymbol{F}_N^* \otimes \boldsymbol{I}_M)$ on $\boldsymbol{y}$ as

$$
\begin{aligned}
\boldsymbol{y}\boldsymbol{A}&(\boldsymbol{F}_N^* \otimes \boldsymbol{I}_M) \\
&= (\boldsymbol{z}_{\mathrm{p},0\to Q}, \boldsymbol{z}_0, \boldsymbol{z}_1, \ldots, \boldsymbol{z}_{U-1}, \boldsymbol{z}_{\mathrm{p},-Q\to-1}) + \boldsymbol{\eta}' \quad (8)
\end{aligned}
$$

where $\boldsymbol{\eta}' = \boldsymbol{\eta}\boldsymbol{A}(\boldsymbol{F}_N^* \otimes \boldsymbol{I}_M)$ and

$$
\boldsymbol{A} = \begin{bmatrix} \boldsymbol{I}_{MN} \\ \left(\boldsymbol{I}_{L-1}\boldsymbol{0}_{(L-1)\times(MN-L+1)}\right) \end{bmatrix}
$$

represents the overlap–add operation. Note that $\boldsymbol{z}_{\mathrm{p},0\to Q}, \boldsymbol{z}_u$, and $\boldsymbol{z}_{\mathrm{p},-Q\to-1}$ are vectors of length $(1 + Q)M$, $(P + 2Q)M$, and QM, respectively. The output sequence $\boldsymbol{z}_{\mathrm{p}} = (\boldsymbol{z}_{\mathrm{p},-Q\to-1}, \boldsymbol{z}_{\mathrm{p},0\to Q})$ corresponds to the time- and frequency-spread sequence of $\boldsymbol{p}$ ($\boldsymbol{z}_{\mathrm{p},-Q\to-1}$ and $\boldsymbol{z}_{\mathrm{p},0\to Q}$ correspond to the Doppler scale from $-Q$ to -1 and from 0 to Q, respectively). $\boldsymbol{z}_u$ also corresponds to the time- and
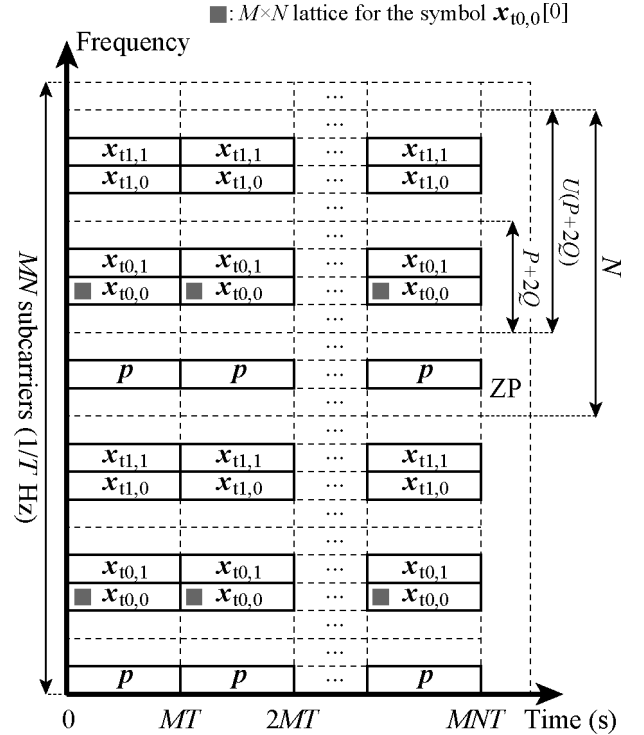
Fig. 4.	Structure of the transmitted signal (D–OSDM) in the time–frequency domain, when $M = 2, P = 2, U = 2,$ and $Q = 1$.

frequency-spread sequence of $\boldsymbol{x}_{tu}$, with a Doppler scale from $-Q$ to Q. In detail, the relationship between $\boldsymbol{z}_{\mathrm{p}}$ and $\boldsymbol{p}$ can be expressed as

$$
\boldsymbol{z}_{\mathrm{p}} = \boldsymbol{p}\left(\boldsymbol{C}_{0,-Q}, \boldsymbol{C}_{0,-Q+1}, \ldots, \boldsymbol{C}_{0,Q}\right) + \boldsymbol{\eta}'_{\mathrm{p}} \quad (9)
$$

where $\boldsymbol{C}_{n,q}$ ($n = 0, 1, \ldots, N-1$) is the channel matrix expressed in

$$
\begin{aligned}
&\boldsymbol{C}_{n,q} \\
&= \begin{pmatrix}
h_{0,q} & W_{MN}^q h_{1,q} & \cdots & W_{MN}^{(M-1)q} h_{M-1,q} \\
W_N^{-n} h_{M-1,q} & W_{MN}^q h_{0,q} & \cdots & W_{MN}^{(M-1)q} h_{M-2,q} \\
\vdots & \vdots & \ddots & \vdots \\
W_N^{-n} h_{1,q} & W_N^{-n} W_{MN}^q h_{2,q} & \cdots & W_{MN}^{(M-1)q} h_{0,q}
\end{pmatrix} \\
&\hspace{9cm} (10)
\end{aligned}
$$

and $\boldsymbol{\eta}'_{\mathrm{p}}$ is a part of $\boldsymbol{\eta}'$. The relationship between $\boldsymbol{z}_u$ and $\boldsymbol{x}_{\mathrm{t}u}$ can be expressed as in (11), shown at the bottom of the page, where $n' = (1 + 2Q) + u(P + 2Q)$. $\boldsymbol{C}_{\mathrm{c}}$ is a matrix of size $PM \times M(P + 2Q)$ and $\boldsymbol{\eta}'_u$ is a sum of two noises, part of $\boldsymbol{\eta}'$ and the channel measurement noise (if an estimated channel is used). From (9) and (11), it is clear that D–OSDM preserves the orthogonality among $\boldsymbol{p}$ and $\boldsymbol{x}_{\mathrm{t}u}$ even after propagation through a doubly spread BEM channel. The proof of (9) and (11) can be found in Appendix A. We would now like to show how the receiver obtains the received message $\boldsymbol{x}_{\mathrm{r}u,p}$.

In D–OSDM, the pilot vector $\boldsymbol{p}$ is shared by both the transmitter and the receiver. The receiver first calculates (8) and obtains the channel impulse response $\boldsymbol{h}_q = (h_{0,q}, h_{1,q}, \ldots, h_{M-1,q})$ by solving (9). Because each element of $\boldsymbol{C}_{n,q}$ in (11) is a product of the channel impulse response $h_{l,q}, W_N^{-n}$, and W_{MN}^q, the receiver can obtain $\boldsymbol{C}_{n,q}$ for all n and q. Finally, the receiver obtains $\boldsymbol{x}_{\mathrm{r}u}$ by solving (11).

In the above paragraph, we ignored the effect of additive noise for simplicity. However, in case we include the noise, (9) and (11) need to be solved using LS. When we perform OSDM communication with a single transmitter and receiver, this can result in a noise enhancement. This is because the condition number of the channel matrix $\boldsymbol{C}_{\mathrm{c}}$ in (11) sometimes becomes large which results in a boost of the noise. To avoid such problems, the use of a multichannel receiver is attractive, as is the case for normal OSDM [26]. More specifically, in that case, the receiver employs K hydrophones ($K \in \mathbb{Z}^+$), and obtains K received sequences, $\boldsymbol{y}^0, \boldsymbol{y}^1, \ldots, \boldsymbol{y}^{K-1}$. The receiver calculates a product of $\boldsymbol{y}^k$ and $\boldsymbol{A}(\boldsymbol{F}_N^* \otimes \boldsymbol{I}_M)$ for all k ($k = 0, 1, \ldots, K - 1$), obtains $\boldsymbol{z}_{\mathrm{p}}^k$ and $\boldsymbol{z}_u^k$, and finally obtains $\boldsymbol{x}_{\mathrm{t}u}$ by solving

$$\begin{aligned}
&\left(\boldsymbol{z}_u^0, \boldsymbol{z}_u^1, \ldots, \boldsymbol{z}_u^{K-1}\right) \\
&= \boldsymbol{x}_{\mathrm{t}u} \left(\boldsymbol{C}_{\mathrm{c}}^0, \boldsymbol{C}_{\mathrm{c}}^1, \ldots, \boldsymbol{C}_{\mathrm{c}}^{K-1}\right) + \left(\boldsymbol{\eta}_u^0, \boldsymbol{\eta}_u^1, \ldots, \boldsymbol{\eta}_u^{K-1}\right) \quad (12)
\end{aligned}$$

in an LS sense, where $\left(\boldsymbol{C}_{\mathrm{c}}^0, \boldsymbol{C}_{\mathrm{c}}^1, \ldots, \boldsymbol{C}_{\mathrm{c}}^{K-1}\right)$ is a matrix of size $PM \times KM(P + 2Q)$. In this case, the receiver obtains a vector of length $MP, \boldsymbol{x}_{\mathrm{t}u}$, from a vector of length $KM(P + Q), (\boldsymbol{z}_u^0, \boldsymbol{z}_u^1, \ldots, \boldsymbol{z}_u^{K-1})$, by using LS for all U groups. Hence, the receiver complexity becomes $\mathcal{O}(M^3)$, as shown in Table I. We found that the condition number of $(\boldsymbol{C}_{\mathrm{c}}^0, \boldsymbol{C}_{\mathrm{c}}^1, \ldots, \boldsymbol{C}_{\mathrm{c}}^{K-1})$ drastically decreases as K increases. In the simulations and experiments that we will carry out in Sections III and IV, we use a multichannel receiver with $K = 3$.

E. D–OSDM Operation at the Receiver With Frequency-Domain Oversampling

As shown in Section II-A, in total, $MN + L - 1$ samples $\boldsymbol{y}$ are obtained which contain useful information about the current block. However, the receiver in Section II-D does not utilize all the information available per block; it utilizes only MN samples, $\boldsymbol{yA}$, for equalization. In this section, we improve the performance of the receiver, based on the frequency-domain oversampling idea proposed in [19].

The receiver obtains an estimate of every transmitted message $\boldsymbol{x}_{\mathrm{t}u,p}$ by applying a frequency-domain oversampling and performing channel equalization, as shown in Fig. 3. The received and frequency-domain oversampled signal of length $2MN, \tilde{\boldsymbol{y}}$, can be expressed as

$$\tilde{\boldsymbol{y}} = \left(\boldsymbol{y}, \boldsymbol{0}_{1 \times (MN-L+1)}\right) \boldsymbol{F}_{2MN}^* \quad (13)$$

$$= \tilde{\boldsymbol{x}} \sum_{q=-Q}^{Q} \tilde{\boldsymbol{H}}_q \boldsymbol{Z}_{2MN}^{2q} + \tilde{\boldsymbol{\eta}} \quad (14)$$

where $\tilde{\boldsymbol{x}}$ is a vector of length $2MN$ given by

$$\tilde{\boldsymbol{x}} = \boldsymbol{x}_{\mathrm{m}}(\boldsymbol{F}_N \otimes \boldsymbol{I}_M, \boldsymbol{0}_{MN \times MN}) \boldsymbol{F}_{2MN}^*$$

and $\tilde{\boldsymbol{H}}_q$ is a matrix of size $2MN \times 2MN$, given by

$$\begin{aligned}
\tilde{\boldsymbol{H}}_q &= \mathrm{diag}\left[\left(\boldsymbol{h}_q, \boldsymbol{0}_{1 \times 2M(N-1)}\right) \boldsymbol{F}_{2MN}^*\right] \\
&= \mathrm{diag}\left(\boldsymbol{h}_q \hat{\boldsymbol{f}}_0^{\mathrm{T}}, \boldsymbol{h}_q \hat{\boldsymbol{f}}_1^{\mathrm{T}}, \ldots, \boldsymbol{h}_q \hat{\boldsymbol{f}}_{2MN-1}^{\mathrm{T}}\right) \quad (15)
\end{aligned}$$

with

$$\hat{\boldsymbol{f}}_r = \left(W_{2MN}^0, W_{2MN}^{-r}, \ldots, W_{2MN}^{-(M-1)r}\right)$$

and, finally

$$\tilde{\boldsymbol{\eta}} = \left(\boldsymbol{\eta}, \boldsymbol{0}_{1 \times (MN-L+1)}\right) \boldsymbol{F}_{2MN}^*. \quad (16)$$

Note that (15) and $\boldsymbol{Z}_{2MN}^{2q}$ represent the effect of channel delay spread (pointwise multiplication of the spectrum of channel delay spread on $\tilde{\boldsymbol{x}}$) and Doppler shift (element shift in the frequency domain), respectively, and the ambient noise $\tilde{\boldsymbol{\eta}}$ is colored by padding zeros on $\boldsymbol{\eta}$. Fig. 5 illustrates the structure of $\tilde{\boldsymbol{y}}$ when $M = 2, P = 2, U = 2, Q = 1$, and $\boldsymbol{h}_q = (1, 0, 0, \ldots, 0)$. As described in (39) in Appendix B, the spectrum of $\boldsymbol{p}, \boldsymbol{x}_{\mathrm{t}0}, \boldsymbol{x}_{\mathrm{t}1}, \ldots, \boldsymbol{x}_{\mathrm{t}U-1}$ in $\tilde{\boldsymbol{x}}$ interfere with each other (ICI) after frequency-domain oversampling. However, we assume that the ICI beyond the direct subcarrier neighbors can be neglected, as done in the D–OFDM case [19]. As shown in this figure, now we have $2MN$ samples in the frequency domain from $MN + L - 1$ useful samples, and the spectra of $\boldsymbol{p}, \boldsymbol{x}_{\mathrm{t}0}, \boldsymbol{x}_{\mathrm{t}1}, \ldots, \boldsymbol{x}_{\mathrm{t}U-1}$ do not interfere with each other even after propagation through doubly spread channels, if we neglect small ICI.

$$\begin{aligned}
\boldsymbol{z}_u &= (\boldsymbol{x}_{\mathrm{t}u,0}, \boldsymbol{x}_{\mathrm{t}u,1}, \ldots, \boldsymbol{x}_{\mathrm{t}u,P-1}) \\
&\times \begin{pmatrix}
\boldsymbol{C}_{n',-Q} & \boldsymbol{C}_{n',-Q+1} & \cdots & \boldsymbol{C}_{n',Q-1} & \boldsymbol{C}_{n',Q} & \boldsymbol{0}_{M \times M} & \cdots & \boldsymbol{0}_{M \times M} \\
\boldsymbol{0}_{M \times M} & \boldsymbol{C}_{n'+1,-Q} & \cdots & \boldsymbol{C}_{n'+1,Q-2} & \boldsymbol{C}_{n'+1,Q-1} & \boldsymbol{C}_{n'+1,Q} & \cdots & \boldsymbol{0}_{M \times M} \\
\vdots & \vdots & \ddots & \vdots & \vdots & \vdots & \ddots & \vdots \\
\boldsymbol{0}_{M \times M} & \boldsymbol{0}_{M \times M} & \cdots & \boldsymbol{0}_{M \times M} & \boldsymbol{C}_{n'+P-1,-Q} & \boldsymbol{C}_{n'+P-1,-Q+1} & \cdots & \boldsymbol{C}_{n'+P-1,Q}
\end{pmatrix} + \boldsymbol{\eta}'_u, \\
&= \boldsymbol{x}_{\mathrm{t}u} \boldsymbol{C}_{\mathrm{c}} + \boldsymbol{\eta}'_u \quad (11)
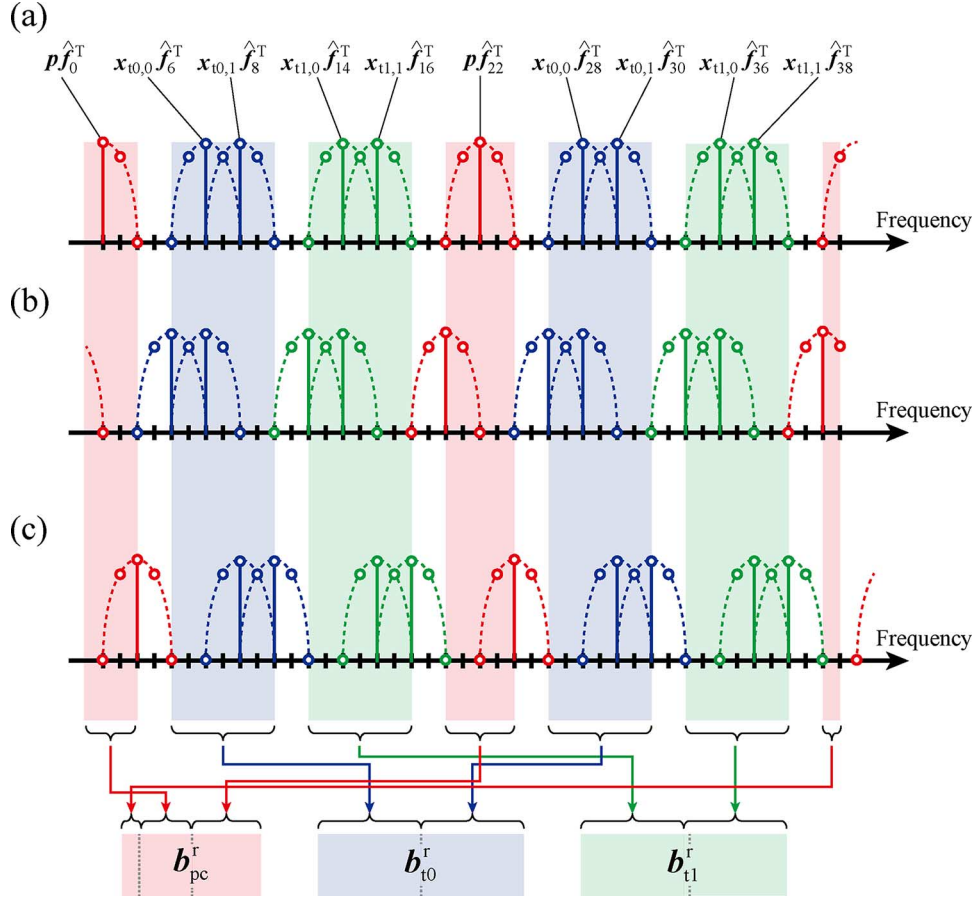\end{aligned}$$

Fig. 5. Structure of $\tilde{y}$ when $M = 2, P = 2, U = 2, Q = 1$, and $\boldsymbol{h}_q = (1, 0, 0, \ldots, 0)$: (a) $q = 0$; (b) $q = -1$; and (c) $q = 1$. Horizontal axes are discretized by $1/(2MNT)$.

The receiver merges oversampled subcarriers on $\tilde{y}$ as

$$\tilde{\boldsymbol{y}}(\boldsymbol{M}_{\mathrm{p}}, \boldsymbol{M}_{\mathrm{t}0}, \boldsymbol{M}_{\mathrm{t}1}, \ldots, \boldsymbol{M}_{\mathrm{t}U-1})$$
$$= (\boldsymbol{b}_{\mathrm{pc}}^{\mathrm{r}}, \boldsymbol{b}_{\mathrm{t}0}^{\mathrm{r}}, \boldsymbol{b}_{\mathrm{t}1}^{\mathrm{r}}, \ldots, \boldsymbol{b}_{\mathrm{t}U-1}^{\mathrm{r}}) \quad (17)$$

where $\boldsymbol{M}_{\mathrm{p}}$ and $\boldsymbol{M}_{\mathrm{t}u}$ are matrices of size $2MN \times M(4Q+1)$ and $2MN \times M[2(P+2Q)-1]$, and they are used to merge subcarriers that carry information about $\boldsymbol{p}$ and $\boldsymbol{x}_{\mathrm{t}u}$, respectively, as shown in Fig. 5. More specifically, we have

$$\boldsymbol{M}_{\mathrm{p}} = \begin{pmatrix} 0 & \boldsymbol{I}_{2Q+1} & \tilde{\boldsymbol{0}}_{\mathrm{p},1} & \tilde{\boldsymbol{0}}_{\mathrm{p},2} & \cdots & \tilde{\boldsymbol{0}}_{\mathrm{p},M-1} \\ 0 & 0 & \boldsymbol{I}_{4Q+1} & \boldsymbol{I}_{4Q+1} & \cdots & \boldsymbol{I}_{4Q+1} \\ \vdots & 0 & 0 & 0 & \cdots & 0 \\ 0 & \vdots & \vdots & \vdots & \ddots & \vdots \\ \boldsymbol{I}_{2Q} & 0 & 0 & 0 & \cdots & 0 \end{pmatrix}$$
$$(18)$$

$$\boldsymbol{M}_{\mathrm{t}u} = \begin{pmatrix} \tilde{\boldsymbol{0}}_{\mathrm{t}u,0} & \tilde{\boldsymbol{0}}_{\mathrm{t}u,1} & \cdots & \tilde{\boldsymbol{0}}_{\mathrm{t}u,M-1} \\ \boldsymbol{I}_{2(P+2Q)+1} & \boldsymbol{I}_{2(P+2Q)+1} & \cdots & \boldsymbol{I}_{2(P+2Q)+1} \\ 0 & 0 & \ddots & 0 \\ \vdots & \vdots & \cdots & \vdots \\ 0 & 0 & \cdots & 0 \end{pmatrix}$$
$$(19)$$

and

$$\tilde{\boldsymbol{0}}_{\mathrm{p},m'} = \boldsymbol{0}_{(m'N-2)\times(4Q+1)}, \qquad m' = 1, 2, \ldots, M-1$$
$$\tilde{\boldsymbol{0}}_{\mathrm{t}u,m} = \boldsymbol{0}_{\{mN+2[1+Q+u(P+2Q)]\}\times[2(P+2Q)-1]}.$$

In this case, the relationship between $\boldsymbol{b}_{\mathrm{pc}}^{\mathrm{r}}$ and $\boldsymbol{p}$ can be approximated as

$$\boldsymbol{b}_{\mathrm{pc}}^{\mathrm{r}} = (\boldsymbol{h}_{-Q}, \boldsymbol{h}_{-Q+1}, \ldots, \boldsymbol{h}_Q)\boldsymbol{P}_{\mathrm{c}} + \tilde{\boldsymbol{\eta}}_{\mathrm{pc}}. \quad (20)$$

Moreover, the relationship between $\boldsymbol{b}_{\mathrm{t}cu}^{\mathrm{r}}$ and $\boldsymbol{x}_{\mathrm{t}u}$ can also be approximated as

$$\boldsymbol{b}_{\mathrm{t}cu}^{\mathrm{r}} = \boldsymbol{x}_{\mathrm{t}u}\boldsymbol{H}_{cu} + \tilde{\boldsymbol{\eta}}_{\mathrm{t}cu} \quad (21)$$

where $\tilde{\boldsymbol{\eta}}_{\mathrm{pc}}$ is a part of $\tilde{\boldsymbol{\eta}}$, and $\tilde{\boldsymbol{\eta}}_{\mathrm{t}cu}$ is a sum of two noises: part of $\tilde{\boldsymbol{\eta}}$ and the channel measurement noise (if an estimated channel is used). $\boldsymbol{P}_{\mathrm{c}}$ and $\boldsymbol{H}_{cu}$ are matrices of size $M(2Q+1)\times M(4Q+1)$ and $MP \times M(2P+4Q-1)$, respectively, and all elements of $\boldsymbol{P}_{\mathrm{c}}$ and $\boldsymbol{H}_{cu}$ are known information (each element of $\boldsymbol{P}_{\mathrm{c}}$ is a product of $\boldsymbol{p}$ and rows of the IDFT matrix, and each element of $\boldsymbol{H}_{cu}$ is a product of $\boldsymbol{h}_q$ and rows of the IDFT matrix). The proof of (20) and (21) can be found in Appendix B. We would now like to show how the receiver with frequency-domain oversampling obtains the received message $\boldsymbol{x}_{\mathrm{r}u}$.

The receiver first performs frequency-domain oversampling using ZP and DFT by computing (13), merges oversampled sub-carriers by computing (17), and obtains $\boldsymbol{h}_q$ by solving (20). Because each element of $\boldsymbol{H}_{cu}$ is a product of the channel impulse response $\boldsymbol{h}_q$ and rows of the IDFT matrix, the receiver can obtain $\boldsymbol{H}_{cu}$ for all u. Finally, the receiver obtains $\boldsymbol{x}_{ru}$ by solving (21). When the receiver employs K hydrophones, the receiver calculates $\tilde{\boldsymbol{y}}^0, \tilde{\boldsymbol{y}}^1, \ldots, \tilde{\boldsymbol{y}}^{K-1}$, obtains $\boldsymbol{b}_{pc}^{rk}$ and $\boldsymbol{b}_{tcu}^r$ for all k, and finally obtains $\boldsymbol{x}_{ru}$ by solving

$$\left(\boldsymbol{b}_{tcu}^{r0}, \boldsymbol{b}_{tcu}^{r1}, \ldots, \boldsymbol{b}_{tcu}^{rK-1}\right) = \boldsymbol{x}_{tu}\left(\boldsymbol{H}_{cu}^0, \boldsymbol{H}_{cu}^1, \ldots, \boldsymbol{H}_{cu}^{K-1}\right)$$
$$+ \left(\tilde{\boldsymbol{\eta}}_{tcu}^0, \tilde{\boldsymbol{\eta}}_{tcu}^1, \ldots, \tilde{\boldsymbol{\eta}}_{tcu}^{K-1}\right). \quad (22)$$

Note that the noise in (22) is colored, because $\tilde{\boldsymbol{\eta}}_{tcu}$ consists of three colored noises: ambient noise, residual ICI, and channel measurement errors. Although this would motivate a weighted LS approach, we still solve (22) in an unweighted LS sense for simplicity. In the following sections, we show that the D–OSDM receiver with frequency-domain oversampling is superior to the D–OSDM receiver without frequency-domain oversampling, even if the noise is colored. In the multiple hydrophone case, the receiver obtains a vector of length MP, $\boldsymbol{x}_{tu}$, from a vector of length $KM(2P + 4Q - 1), (\boldsymbol{b}_{tcu}^{r0}, \boldsymbol{b}_{tcu}^{r1}, \ldots, \boldsymbol{b}_{tcu}^{rK-1})$, by using LS for all U groups. Hence, the receiver complexity becomes $\mathcal{O}(M^3)$, as shown in Table I. Note, however, that the complexity of the D–OSDM receiver with frequency-domain oversampling doubles compared to the D–OSDM receiver without frequency-domain oversampling. However, we can utilize all the information available per block. Hence, the performance of the D–OSDM receiver with frequency-domain oversampling is expected to be superior to that of the D–OSDM receiver without frequency-domain oversampling.

F. Characteristics of D–OSDM

In this section, we present the characteristics of D–OSDM, by comparing it to D–OFDM. The advantages of D–OSDM over D–OFDM are the low dynamic range of the transmitted signal and a better communication quality, in exchange for receiver complexity. Fig. 6 shows the peak-to-average power ratio (PAPR) of D–OSDM and D–OFDM. The D–OSDM signal is a sum of one pilot data vector and PU data vectors, hence, the maximum PAPR of D–OSDM becomes $PU + 1$. On the other hand, the D–OFDM signal is a sum of M pilot symbols and MPU data symbols, which results in a large PAPR, as shown in Fig. 6. As a result, D–OSDM is attractive compared to D–OFDM in terms of PAPR, which can result in a signal-to-noise ratio (SNR) gain in practical situations where the nonlinearity of the power amplifier at the transmitter should be avoided.

Moreover, in heavy multipath channels, the channel frequency characteristics face severe fading at specific frequencies of subcarriers. In D–OFDM, the complex-valued data symbols are assigned to specific subcarriers, hence, if the channel frequency characteristic has a null at a subcarrier, the associated information may be lost due to the low SNR on that subcarrier, a drawback that comes with the advantage of a low complexity
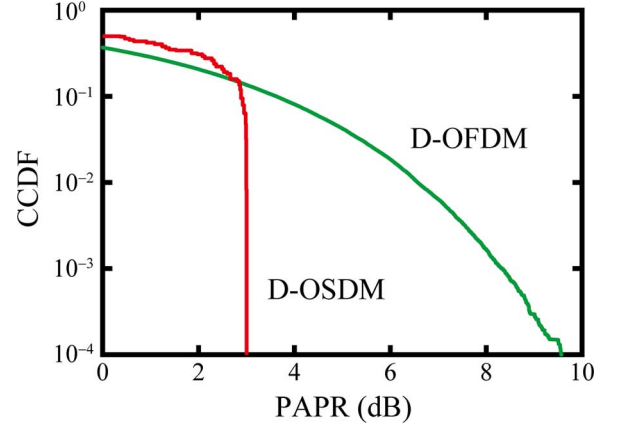

Fig. 6. PAPR of D–OSDM and D–OFDM, when $M = 63, P = 1, U = 1$, and $Q = 1$.

at the receiver. Different from D–OFDM, the pilot and data subcarriers appear M times in D–OSDM, hence, D–OSDM exploits the full diversity of the channel and we can avoid a low SNR scenario at specific pilot/data subcarriers for a similar channel environment. Because there is a nonlinear relationship between the SNR and BER, the communication quality of D–OSDM is expected to be better than that of D–OFDM in the same environment.

However, the receiver complexity of D–OSDM with frequency-domain oversampling becomes M^2 times larger than that of D–OFDM with frequency-domain oversampling, as shown in Table I. This is because D–OSDM has to solve a large-size problem [as shown in (12) and (22)] compared to D–OFDM.

III. PERFORMANCE EVALUATION BY SIMULATIONS

A. Simulation Environment

We first evaluate the performance of D–OSDM under doubly spread channels by simulations. Table II shows the parameters used in the simulations. We consider three cases.

Case 1) We compare the performance of normal OSDM and D–OSDM, under the same block length, data rate, and signal bandwidth, to illustrate the benefits of D–OSDM. The parameters are designed to make the block length as small as possible in order to minimize the effect of the Doppler spread.

Case 2) We consider the use of a larger value of P and U for D–OSDM, to check the relationship between the effective data rate and the resilience against Doppler spread. A Reed–Solomon (RS) code is employed to compare different D–OSDM schemes under the same effective data rate. Based on the results obtained in Case 1), we only consider the receiver with frequency-domain oversampling.

Case 3) We compare the performance of D–OSDM and D–OFDM, under the same block length, data rate, and signal bandwidth. As in Case 2), an RS code is employed. Based on the results obtained in Cases 1) and 2), we choose $P = 1$ and use the receiver with frequency-domain oversampling.

TABLE II
PARAMETER SETTINGS FOR THE SIMULATIONS AND EXPERIMENTS

	Type	Parameters		Coding	Performances				
Case 1),	OSDM	M	189	Turbo	Block length (ms):	87.6			
		P	1		Modulation:	QPSK ($b=2$)			
		Q	0		Code rate c_{rate}:	1/3			
		U	1		Data rate (kbps):	1.4			
		L	60		Signal bandwidth (kHz):	5			
	D-OSDM with/without frequency-domain oversampling	M	63	N/A	Block length (ms):	87.6			
		P	1		Modulation:	QPSK ($b=2$)			
		Q	1		Code rate c_{rate}:	1			
		U	1		Data rate (kbps):	1.4			
		L	60		Signal bandwidth (kHz):	5			
Case 2),	D-OSDM with frequency-domain oversampling			RS		$P=1$	$P=2$	$P=3$	
		M	63		Block length (ms):	87.6	100.2	112.8	$U=1$
						163.2	201.0	238.8	$U=3$
		P	1, 2, 3		Modulation:	16QAM ($b=4$)			
		Q	1		Code rate c_{rate}:	4/5	7/15	1/3	$U=1$
		U	1, 3			8/15	1/3	4/15	$U=3$
		L	60		Data rate (kbps):	2.3	2.3	2.2	$U=1$
						2.4	2.5	2.5	$U=3$
					Signal bandwidth (kHz):	5	5	5	
Case 3).	D-OSDM and D-OFDM with frequency-domain oversampling	M	63	RS	Block length:	87.6 ms			
		P	1		Modulation:	16QAM ($b=4$)			
		Q	1		Code rate c_{rate}:	4/5			
		U	1		Data rate (kbps):	2.3			
		L	60		Signal bandwidth (kHz):	5			

The receiver is assumed to have three hydrophones ($K = 3$). The performances of the communication schemes are evaluated by calculating the relationship among the maximum Doppler shift f_{d}, the energy per bit to noise power spectral density ratio E_b/N_0, and BER [in Case 1)] or the block error ratio (BLER) [in Cases 2 and 3)]. The normalized Doppler shift $f_{\text{d}}MNT$ is also provided as well as the maximum Doppler shift. In the simulations, E_b/N_0 is defined as $\sigma_{\text{s}}^2/(\sigma_{\text{n}}^2 D_{\text{rate}})$, where $\sigma_{\text{s}}^2, \sigma_{\text{n}}^2$, and D_{rate} are the power of the received sequence without noise, the power of the noise that is added to the received sequence, and the data rate shown in Table II, respectively.

For the simulations, we use an equivalent baseband model, whose time-domain resolution T is 0.2 ms. The channel impulse response is assumed to be Rayleigh-distributed, exponentially decaying (0.66 dB per tap in power), with a maximum delay spread of 12 ms, resulting in $L = 60$ taps. The channels from the transmitter to all the hydrophones are assumed to be mutually independent. The channel Doppler spread is modeled by a bell-shaped function

$$S(f) = \frac{\sqrt{a}}{\pi f_{\text{d}} \left\{ 1 + a \left(\frac{f}{f_{\text{d}}} \right) \right\}}, \qquad |f| \leq f_{\text{d}} \qquad (23)$$

where a is a positive scalar and assumed to be 9 in this paper. The message consists of random, QPSK-modulated symbols.

After calculating the effect of the delay and Doppler spread, Gaussian noise is added to the signal, and the demodulation processes are carried out.

B. Simulation Results

We evaluate the performance of D–OSDM from two viewpoints. First, the relationship between the maximum Doppler shift f_{d} and BER/BLER is presented to show the robustness of D–OSDM to doubly spread channels. Then, the relationship between E_b/N_0 and BER/BLER is studied to illustrate the performance of D–OSDM in practical scenarios.

Let us first focus on a performance comparison between D–OSDM and normal OSDM [Case 1)]. Figs. 7 and 8 show the relationship between f_{d} and BER and the relationship between E_b/N_0 and BER for D–OSDM and normal OSDM, respectively. It can be seen that D–OSDM in doubly spread channels achieves a better performance than OSDM in a high-SNR environment, somewhere above 20 dB (Fig. 7), and in a large-Doppler-spread environment, somewhere above 10 Hz (Fig. 8). On the other hand, OSDM achieves a better performance when E_b/N_0 is less than 20 dB and the maximum Doppler shift is less than 10 Hz [Figs. 7(c) and 8(a)]. This means that D–OSDM works effectively under doubly spread channels in high-SNR environments, but OSDM remains attractive when the SNR is low and
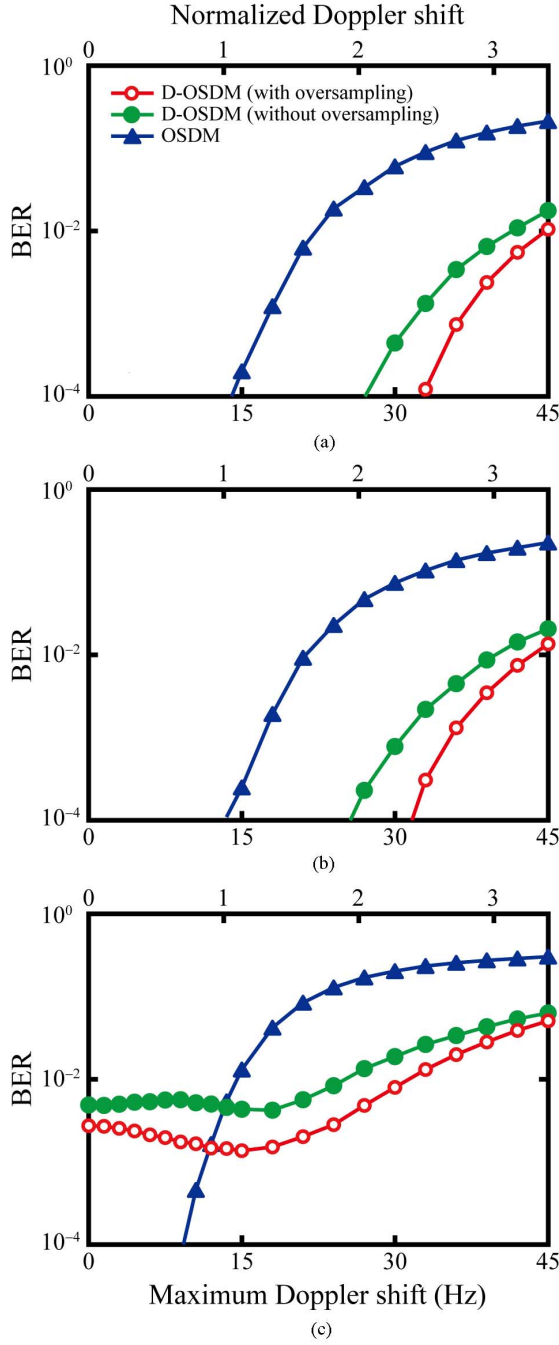
Fig. 7. Relationship between the maximum Doppler shift and BER in simulation [Case 1)]: (a) $E_b/N_0 = 30$ dB; (b) $E_b/N_0 = 20$ dB; and (c) $E_b/N_0 = 10$ dB.

Fig. 8. Relationship between E_b/N_0 and BER in simulation [Case 1)]: (a) maximum Doppler shift of 10 Hz; (b) maximum Doppler shift of 15 Hz; and (c) maximum Doppler shift of 20 Hz.

f_d is small. Let us also compare the performances of D–OSDM without frequency-domain oversampling and D–OSDM with frequency-domain oversampling. It can be seen from Figs. 7 and 8 that D–OSDM with frequency-domain oversampling exceeds D–OSDM without frequency-domain oversampling for all scenarios [$10 \le E_b/N_0 \le 30$ (dB) and $0 \le f_\mathrm{d} \le 45$ (Hz)]. This means that we can improve the performance of D–OSDM using frequency-domain oversampling because we can utilize all the information available per block, as discussed in Section II-E. Hence, we adopt D–OSDM with frequency-domain oversampling in the remainder of this section.

Let us next focus on a performance comparison among different D–OSDM schemes [Case 2)]. Figs. 9 and 10 show the relationship between f_d and BLER as well as the relationship between E_b/N_0 and BLER for D–OSDM with frequency-domain oversampling ($P = 1, 2,$ and 3, and, $U = 1$ and 3), respectively. Focusing on the $U = 1$ case (solid line), it can be seen that D–OSDM ($P = 1$) in doubly spread channels achieves a better performance than D–OSDM ($P = 2$ and 3) in a high-SNR environment, somewhere above 20 dB (Fig. 9), regardless of f_d (Fig. 10). D–OSDM ($P = 2$ and 3) sometimes exceeds ($P = 1$) in a low-SNR environment, however, BLER remains more than 10^{-2} which is not sufficient for practical communication. Focusing on the $U = 3$ case (dotted line), it can be seen that D–OSDM ($P = 1$) in doubly spread channels achieves a better

Fig. 9. Relationship between the maximum Doppler shift and BLER in simulation [Case 2]: (a) $E_b/N_0 = 30$ dB; (b) $E_b/N_0 = 20$ dB; and (c) $E_b/N_0 = 10$ dB.
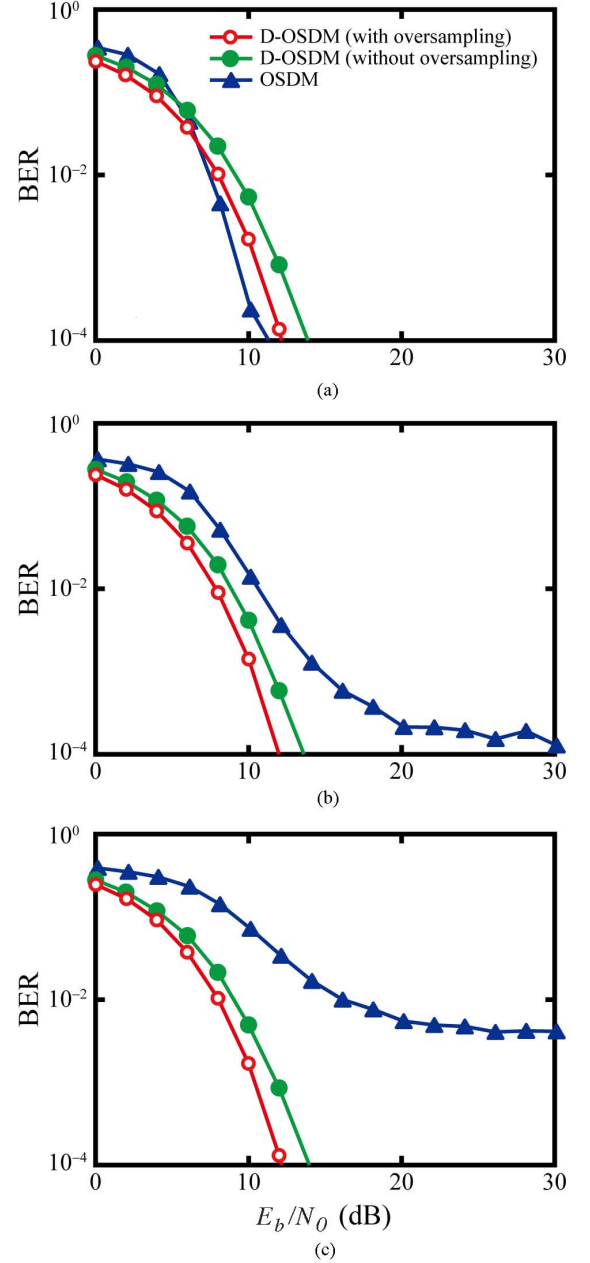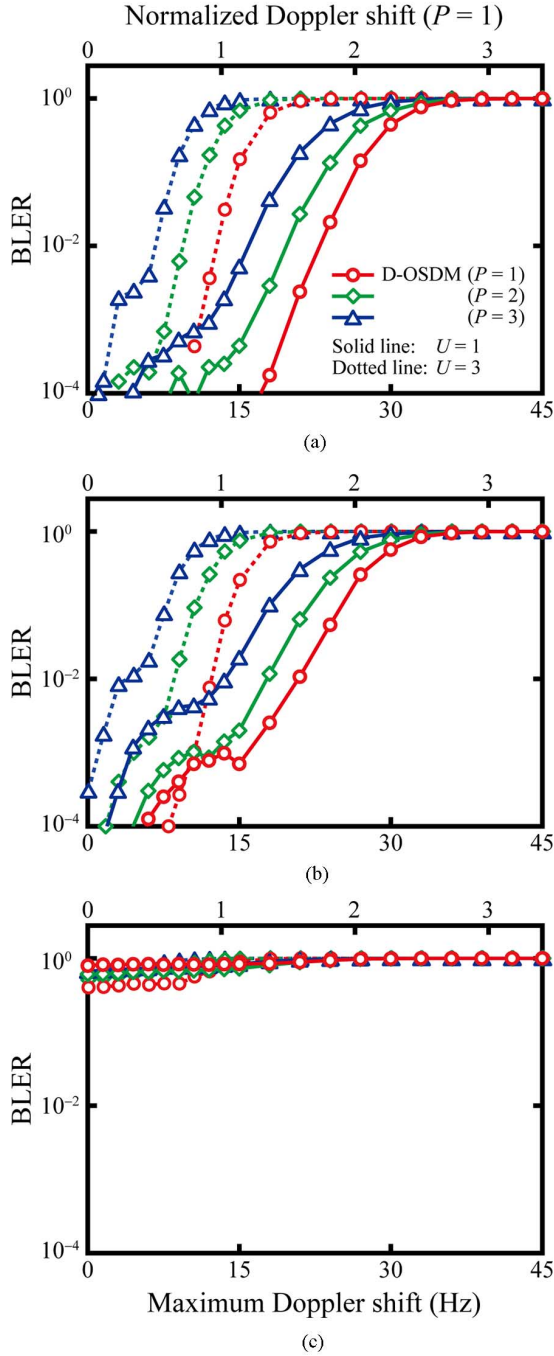

Fig. 10. Relationship between E_b/N_0 and BLER in simulation [Case 2]: (a) maximum Doppler shift of 10 Hz; (b) maximum Doppler shift of 15 Hz; and (c) maximum Doppler shift of 20 Hz.

performance than D–OSDM ($P = 2$ and 3) in a high-SNR environment, as for the $U = 1$ case. However, it can also be seen that the performance of D–OSDM ($U = 3$) does not exceed that of D–OSDM ($U = 1$), especially in a large Doppler spread environment. Therefore, D–OSDM ($P = 1$) works well under Doppler spread and can provide reliable communication even in doubly spread channels, and is therefore a rational choice for practical UWA communication (e.g., when the required BLER is less than 10^{-3}).

We also would like to investigate the performance difference between D–OSDM and D–OFDM [Case 2]. Figs. 11 and 12

show the relationship between f_d and BLER and the relationship between E_b/N_0 and BLER for D–OSDM and D–OFDM, respectively. It is shown that D–OSDM in doubly spread channels achieves a better performance than D–OFDM under the same circumstances. More specifically, to achieve a BLER of 10^{-3}, D–OSDM can handle a maximum f_d that is about 20 Hz larger (about 1.5 larger in normalized Doppler shift) compared to D–OFDM (see Figs. 11(a) and (b)). As a result, D–OSDM achieves a BLER of 10^{-3} in a high-SNR environment when f_d is less than 20 Hz (Figs. 12(a) and (b)) although D–OFDM has a BLER floor around 10^{-2}. In Fig. 12(c) both D–OSDM and D–OFDM have a BLER floor, but BLER of D–OSDM is about 1/10th compared to that of D–OFDM. This performance difference is attractive because this means that D–OSDM can provide

Fig. 11. Relationship between the maximum Doppler shift and BLER in simulation [Case 3)]: (a) $E_b/N_0 = 30$ dB; (b) $E_b/N_0 = 20$ dB; and (c) $E_b/N_0 = 10$ dB.
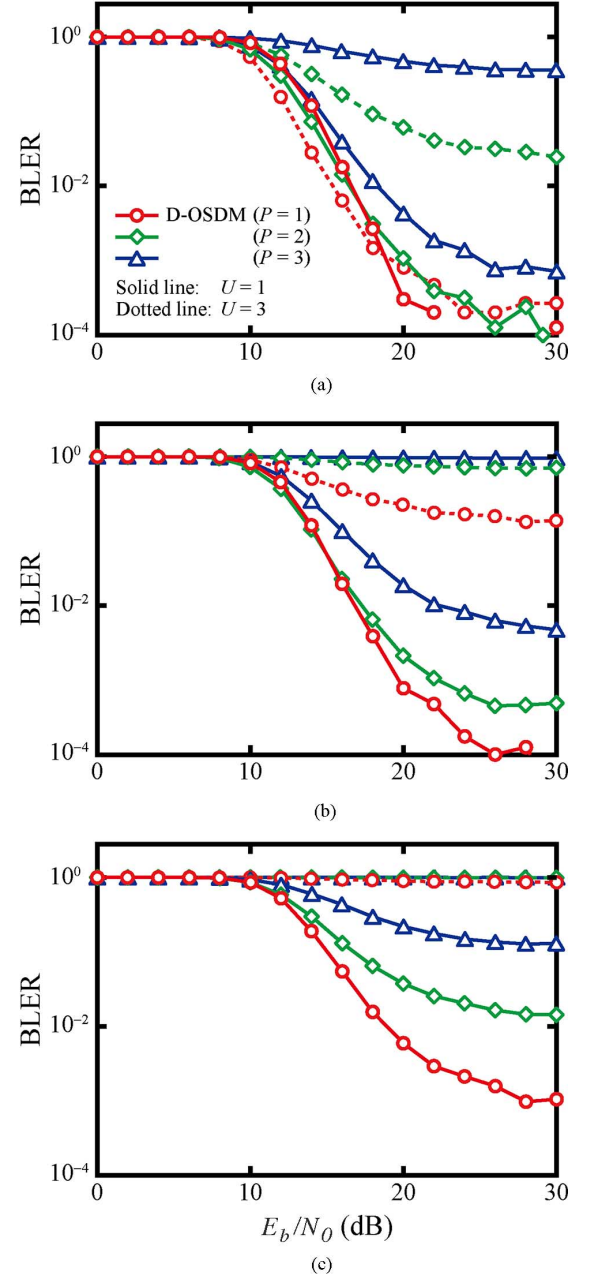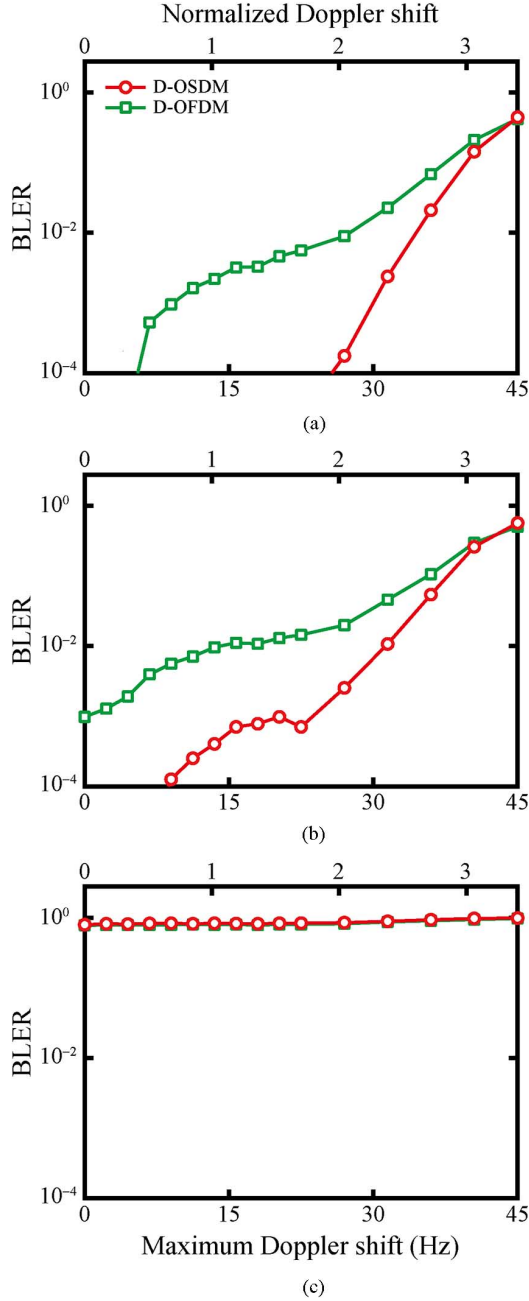

Fig. 12. Relationship between E_b/N_0 and BLER in simulation [Case 3)]: (a) maximum Doppler shift of 10 Hz; (b) maximum Doppler shift of 15 Hz; and (c) maximum Doppler shift of 20 Hz.

the same communication quality as D–OFDM but with a lower signal power. Note that this increase of the power efficiency improves as the required communication quality increases.

To conclude this part, D–OSDM is more attractive than OSDM for UWA communication in doubly spread channels; D–OSDM also works effectively under channels with large delay and Doppler spreads in high-SNR environments, but OSDM (with Turbo coding) remains attractive under channels with a small Doppler spread or when the SNR is low. Moreover, we found that D–OSDM with frequency-domain oversampling and $P = 1$ and $U = 1$ is a rational choice for practical UWA communication; it works well under Doppler spread and can provide reliable communication even in doubly spread channels.

D–OSDM has also advantages over D–OFDM; D–OSDM can handle a larger f_d or a smaller E_b/N_0 compared to D–OFDM to achieve the same BLER. What was found in these simulations was that D–OSDM can achieve the same BER compared to all other schemes but using a lower signal power, especially in high-SNR environments with large Doppler spreads. Because UWA modems are usually battery operated (e.g., since they are mounted on underwater vehicles that work as a hub in underwater acoustic networks), the signal power reduction by D–OSDM is attractive, since it increases the operation time. On top of this, D–OSDM is characterized by a low PAPR.

IV. PERFORMANCE EVALUATION IN EXPERIMENTS

A. Experimental Environment

To evaluate the performance of D–OSDM in a realistic environment, we conduct some experiments in a test tank,

Fig. 13. Experimental conditions: (a) testing environment, (b) obtained channel impulse response, and (c) obtained Doppler spread (solid line) and Doppler spread model used in simulation (dotted line).

Fig. 14. Exemplary channel obtained from the experiment: (a) delay-Doppler representation; and (b) related channel impulse responses at different relative Doppler shifts.

equipped with a wave generator. The moving surface (wave) created by the wave generator is used to generate a dynamic, doubly spread channel [see Fig. 13(a)]. The test tank has width, height, and depth of 12 000, 400, and 200 mm, respectively. When the channel is static, the water level (WL) is set to 250 mm. When surface waves are generated, the wave length and the wave height are 1090 and 90 mm, respectively. Since the test tank has a wave absorber on the left-hand side, the wave status is static throughout the experiments.

We place one transducer (H1a, Aquarian audio products, Anacortes, WA, USA) and four hydrophones (H2a, Aquarian audio products) in the test tank. They are tightly fixed so

that they do not move by the wave during the experiments. Both the transducer and the hydrophones are connected to a digital-to-analog/analog-to-digital (DA/AD) converter (USB-6366, National Instruments, Austin, TX, USA), with a sampling rate of 160 kHz, and work respectively as a transmitter (Tx) and a receiver (Rx). Because there are four hydrophones at Rx, we can calculate four BER/BLERs from a single trial [the number of combinations of three signals ($K = 3$) out of four].

Fig. 13(b) shows a channel impulse response obtained from the experiments. This figure is obtained by transmitting a linear frequency modulated signal (from 15 to 25 kHz) of length 8.5 s, and by calculating the cross correlation between the transmitted
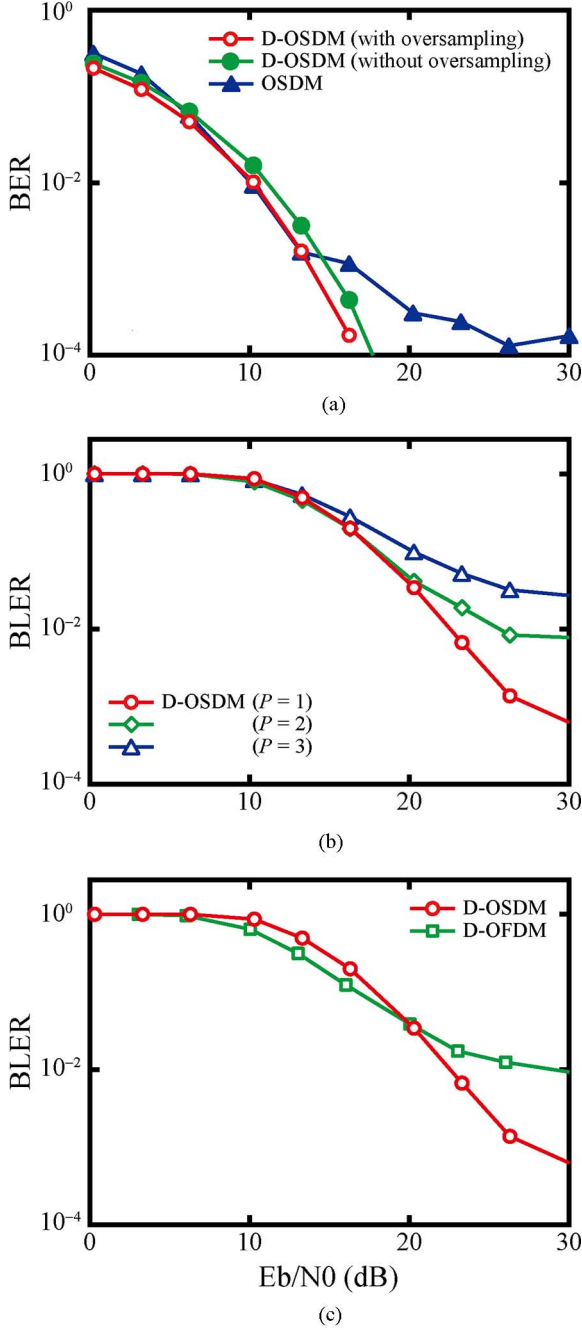
Fig. 15. Relationship between E_b/N_0 and BER/BLER in the experiment: (a) Case 1); (b) Case 2); and (c) Case 3).

and received signals, when there are no surface waves. The power of the signal decays exponentially, and we can observe two peaks, which respectively correspond to the direct signal from the transducer and the reflected signal from the right-hand side wall of the test tank. The channel delay spread, which determines L, is assumed to be 12 ms, the point where the signal power decays about 40 dB from its peak.

Fig. 13(c) (solid line) shows a Doppler spread profile, obtained from the experiments. This figure is obtained by transmitting a single tone of 20 kHz (corresponding to the carrier frequency of the signal) for 0.84 s (corresponding to the period of the surface wave) and by performing a Fourier transform of

the received signal. The obtained spectrum is clearly spread, however, it also shows a sharp peak on the carrier frequency. This is because there is a line of sight between Tx and Rx. The transmitted signal originating from Tx propagates toward Rx with reflections from both the water surface and the floor of the test tank, and Doppler shifts occur whenever the signal is reflected at the water surface due to the movement of the surface wave. However, the direct signal path from Tx to Rx and the path from Tx to Rx via the right-hand side wall are not affected by Doppler shifts, which results in a sharp peak of the frequency spectrum at the carrier frequency. As a result, the experimental conditions should be modeled as a combination of two propagation models: a two-path Rayleigh fading channel with no Doppler spread, and a multipath Rayleigh fading channel with a Gaussian-shaped Doppler spread, as shown in Fig. 13(c) (dotted line). The Gaussian-shaped Doppler spread function is assumed to have a maximum Doppler shift of 20 Hz and a standard deviation of 8 Hz. The signal powers that propagate over the two-path model and the multipath model are assumed to be equal. This model matches the experimental results well, when we perform simulations to confirm the experimental results, as will be demonstrated in Section IV-B.

Fig. 14 shows an exemplary channel obtained from the experiment. Fig. 14(a) shows the delay-Doppler representation of the channel. This figure was obtained by transmitting a D–OSDM signal (with $M = 63, P = 1, U = 1$, and $Q = 9$), and calculating the channel impulse responses by (20) for $q = -9, -8, \ldots, 9$ from the received signal. The relative Doppler shift [when we use the parameters in Table II, Case 3)] is also shown in this figure. As is clear from this figure, the channel has a large Doppler spread in the frequency domain. Fig. 14(b) shows the related channel impulse responses obtained by transmitting a D–OSDM signal (with $M = 63, P = 1, U = 1$, and $Q = 1$), and calculating the channel impulse responses by (20) for $q = -1, 0$, and 1 from the received signal. As shown in this figure, D–OSDM succeeds to extract the channel impulse responses at different Doppler shifts, which are related to the intersections of the delay-Doppler representation in Fig. 14(a) at the relative Doppler shifts $-1, 0$, and 1.

In such an environment, we perform UWA communication using D–OSDM, whose signal parameters are the same as in the earlier simulations (see Table II). However, in Case 2), we only compare the performance of D–OSDM schemes with $U = 1$, since the simulations showed that this choice achieves the best results. The carrier frequency of the communication signal is set to 20 kHz. As benchmarks, we also consider UWA communication using normal OSDM (with Turbo coding), and D–OFDM. In D–OFDM, we use rectangular pulse shaping instead of raised-cosine pulse shaping [19]. The performance of the communication schemes is evaluated by calculating the relationship between E_b/N_0 and BER, by changing the signal power. In the experiments, E_b/N_0 is defined as $(\sigma_s^2 - \sigma_n^2)/(\sigma_n^2 D_{\text{rate}})$, where σ_s^2, σ_n^2, and D_{rate} are the power of the received sequence (with noise), the power of the noise (observed signal when there is no communication signal), and the data rate shown in Table II, respectively. Simulations using the combination of the two propagation models discussed earlier are also conducted to confirm the experimental results.
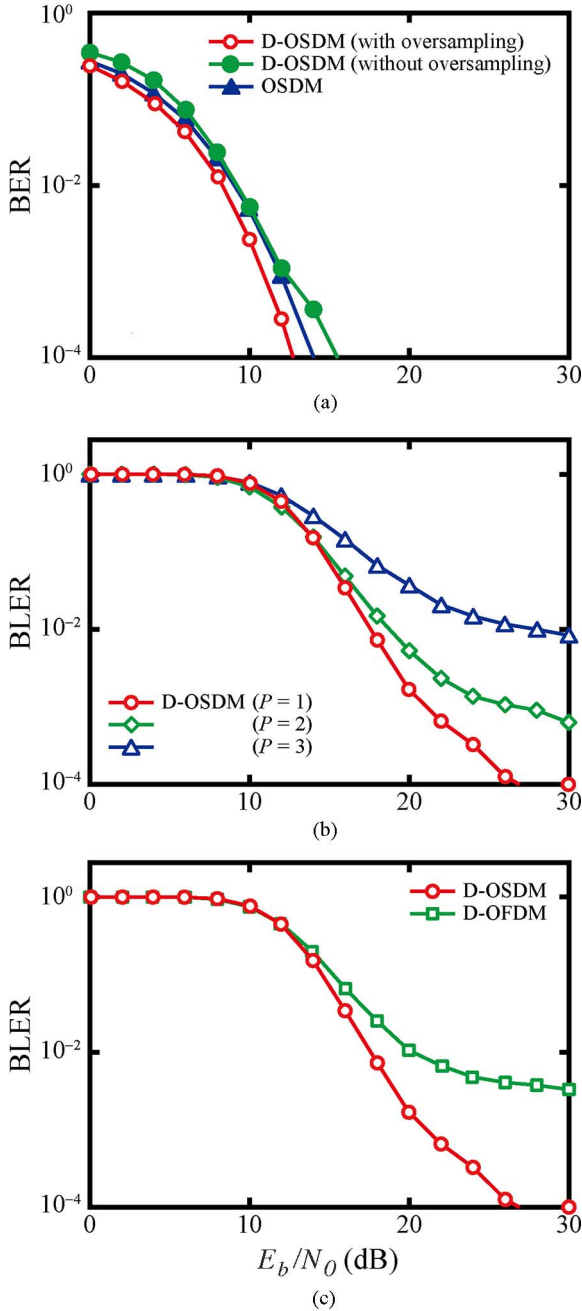
Fig. 16.　Relationship between E_b/N_0 and BER/BLER in simulation: (a) Case 1); (b) Case 2); and (c) Case 3).

B. Experimental Results

Figs. 15 and 16 show the relationship between E_b/N_0 and BER/BLER of D–OSDM, normal OSDM, and D–OFDM, obtained by the experiment and simulation, respectively. Note that the simulation results were obtained using the new model described in Section IV-A.

We first focus on the performance comparison between D–OSDM and normal OSDM [Case 1)] [Figs. 15(a) and 16(a)]. It can be observed that D–OSDM achieves a better performance than normal OSDM in a high-SNR environment. For example, D–OSDM achieves BER of 10^{-3} at E_b/N_0 of 14 dB, while normal OSDM achieves the same BER at E_b/N_0 of only 17

dB. It is also clear that D–OSDM with frequency-domain oversampling exceeds D–OSDM without frequency-domain oversampling. The simulation results also show the same tendency as the experimental results.

We next focus on different D–OSDM schemes [Case 2)] [Figs. 15(b) and 16(b)]. As also illustrated by the results of Section III-B, we note that D–OSDM ($P = 1$) in doubly spread channels achieves a better performance than D–OSDM ($P = 2$ and 3) in a high-SNR environment. This means that D–OSDM ($P = 1$) works well under Doppler spread and can provide reliable communication even in doubly spread channels, and remains a rational choice for practical UWA communication.

We also compare D–OSDM with D–OFDM [Case 3)] [Figs. 15(c) and 16(c)]. It is seen that D–OSDM in doubly spread channels achieves a better performance than D–OFDM in high-SNR environments, somewhere above 20 dB, and can improve BLER at the same E_b/N_0. More specifically, D–OSDM achieves BLER of 10^{-3} when $E_b/N_0 = 30$ dB, although D–OFDM has a BLER floor around 10^{-2} in the experiment. The simulation results also show the same tendency as the experimental results.

In summary, as in Section III, D–OSDM is found to be more attractive than normal OSDM and D–OFDM for UWA communication in doubly spread channels, in exchange for receiver complexity. Different from Section III, in this section, the channel has a line-of-sight component, which allows us to analyze the performance of D–OSDM in doubly spread channels with line-of-sight conditions. We can conclude that D–OSDM achieves a better performance than OSDM and D–OFDM, and that it provides a reliable communication link even in doubly spread channels with a line-of-sight component. The simulation results conducted on this new channel model match the experimental results well. The obtained results suggest that D–OSDM can provide low-power and high-quality UWA communication in realistic doubly spread channels.

V. CONCLUSION

We have proposed D–OSDM as a viable alternative offering a highly reliable and flexible communication scheme for UWA communication under delay and Doppler spread. D–OSDM is a combination of the OSDM technique and orthogonal multiple access, which are perfectly complementary; orthogonal multiple access provides OSDM the robustness to Doppler spread, while OSDM provides orthogonal multiple access accurate channel sensing. We have presented the required D–OSDM signal processing steps both at the transmitter and the receiver, and we have highlighted the characteristics of D–OSDM in comparison to existing schemes. We have also evaluated the performance of D–OSDM by both simulations and test-tank experiments. The obtained results suggest that D–OSDM can provide a low-power and high-quality UWA communication link especially in channels with large delay and Doppler spreads; D–OSDM improves E_b/N_0 compared to other communication schemes to achieve the same BER in high-SNR environments. Because most underwater systems are battery operated, D–OSDM is expected to be attractive because it can increase the lifetime of the system. We believe that D–OSDM can become a powerful communication tool for underwater operations.

APPENDIX A
PROOF OF (9) AND (11)

Focusing on the left-hand side of (8), we can obtain

$$
\begin{aligned}
&\boldsymbol{y}\boldsymbol{A}\left(\boldsymbol{F}_N^* \otimes \boldsymbol{I}_M\right) \\
&= \boldsymbol{x}\left(\sum_{q=-Q}^{Q} \boldsymbol{H}_q \boldsymbol{\Lambda}_q\right)\boldsymbol{A}\left(\boldsymbol{F}_N^* \otimes \boldsymbol{I}_M\right) + \boldsymbol{\eta}' \\
&= \boldsymbol{x}_{\mathrm{m}}\left(\boldsymbol{F}_N \otimes \boldsymbol{I}_M\right)\left(\sum_{q=-Q}^{Q} \boldsymbol{H}'_q \boldsymbol{\Lambda}'_q\right)\left(\boldsymbol{F}_N^* \otimes \boldsymbol{I}_M\right) + \boldsymbol{\eta}'
\end{aligned}
$$

$$(24)$$

where

$$
\begin{aligned}
\boldsymbol{H}'_q &= \boldsymbol{H}_q \boldsymbol{A} \\
&= \begin{pmatrix}
h_{0,q} & h_{1,q} & \cdots & h_{MN-1,q} \\
h_{MN-1,q} & h_{0,q} & \cdots & h_{MN-2,q} \\
\vdots & \vdots & \ddots & \vdots \\
h_{1,q} & h_{2,q} & \cdots & h_{0,q}
\end{pmatrix}
\end{aligned}
$$

$$(25)$$

$$
\boldsymbol{\Lambda}'_q = \operatorname{diag}\left(W_{MN}^0, W_{MN}^q, \ldots, W_{MN}^{(MN-1)q}\right). \quad (26)
$$

Note that $\boldsymbol{H}'_q$ can be defined as

$$
\boldsymbol{H}'_q = \left(\boldsymbol{I}_N \otimes \boldsymbol{H}_{\mathrm{U},q}\right) + \left(\boldsymbol{Z}_N \otimes \boldsymbol{H}_{\mathrm{L},q}\right) \quad (27)
$$

where $\boldsymbol{H}_{\mathrm{U}}$ and $\boldsymbol{H}_{\mathrm{L}}$ are the $M \times M$ matrices given by

$$
\boldsymbol{H}_{\mathrm{U},q} = \begin{pmatrix}
h_{0,q} & h_{1,q} & h_{2,q} & \cdots & h_{M-1,q} \\
0 & h_{0,q} & h_{1,q} & \cdots & h_{M-2,q} \\
\vdots & \vdots & \vdots & \ddots & \vdots \\
0 & 0 & 0 & \cdots & h_{1,q} \\
0 & 0 & 0 & \cdots & h_{0,q}
\end{pmatrix} \quad (28)
$$

and

$$
\boldsymbol{H}_{\mathrm{L},q} = \begin{pmatrix}
0 & 0 & 0 & \cdots & 0 \\
h_{M-1,q} & 0 & 0 & \cdots & 0 \\
\vdots & \vdots & \vdots & \ddots & \vdots \\
h_{2,q} & h_{3,q} & h_{4,q} & \cdots & 0 \\
h_{1,q} & h_{2,q} & h_{3,q} & \cdots & 0
\end{pmatrix}. \quad (29)
$$

The right-hand side of (24) can be simplified by using

$$
\begin{aligned}
&\left(\boldsymbol{F}_N \otimes \boldsymbol{I}_M\right)\boldsymbol{H}'_q \boldsymbol{\Lambda}'_q \left(\boldsymbol{F}_N^* \otimes \boldsymbol{I}_M\right) \\
&= \boldsymbol{H}_q^{\mathrm{c}} \boldsymbol{\Lambda}'_q \left(\boldsymbol{F}_N^* \otimes \boldsymbol{I}_M\right) \\
&= \boldsymbol{H}_q^{\mathrm{c}} \left(\boldsymbol{\Lambda}_{\mathrm{L},q} \otimes \boldsymbol{\Lambda}_{\mathrm{R},q}\right)\left(\boldsymbol{F}_N^* \otimes \boldsymbol{I}_M\right) \\
&= \boldsymbol{H}_q^{\mathrm{c}} \left(\boldsymbol{\Lambda}_{\mathrm{L},q}\boldsymbol{F}_N^* \otimes \boldsymbol{\Lambda}_{\mathrm{R},q}\right)
\end{aligned}
$$

$$(30)$$

where

$$
\boldsymbol{H}_q^{\mathrm{c}} = \boldsymbol{F}_N \otimes \boldsymbol{H}_{\mathrm{U},q} + \left(\boldsymbol{F}_N \boldsymbol{Z}_N\right) \otimes \boldsymbol{H}_{\mathrm{L},q} \quad (31)
$$

$$
\boldsymbol{\Lambda}_{\mathrm{L},q} = \operatorname{diag}\left(W_N^0, W_N^q, \ldots, W_N^{(N-1)q}\right) \quad (32)
$$

$$
\boldsymbol{\Lambda}_{\mathrm{R},q} = \operatorname{diag}\left(W_{MN}^0, W_{MN}^q, \ldots, W_{MN}^{(M-1)q}\right). \quad (33)
$$

$\boldsymbol{\Lambda}_{\mathrm{L},q}\boldsymbol{F}_N^*$ becomes a column-shifted DFT matrix as shown in

$$
\begin{aligned}
&\boldsymbol{\Lambda}_{\mathrm{L},q}\boldsymbol{F}_N^* \\
&= \begin{pmatrix}
W_N^0 & W_N^0 & \cdots & W_N^0 \\
W_N^q & W_N^{-1+q} & \cdots & W_N^{-N+q} \\
\vdots & \vdots & \ddots & \vdots \\
W_N^{(N-1)q} & W_N^{-(N-1)+(N-1)q} & \cdots & W_N^{-(N-1)^2+(N-1)q}
\end{pmatrix}
\end{aligned}
$$

$$(34)$$

and $\boldsymbol{\Lambda}_{\mathrm{L},q}\boldsymbol{F}_N^* \otimes \boldsymbol{\Lambda}_{\mathrm{R},q}$ becomes (35), shown at the bottom of the page. As a result, (30) becomes

$$
\begin{aligned}
&\boldsymbol{H}_q^{\mathrm{c}}\left(\boldsymbol{\Lambda}_{\mathrm{L},q}\boldsymbol{F}_N^* \otimes \boldsymbol{\Lambda}_{\mathrm{R},q}\boldsymbol{I}_M\right) \\
&\qquad = \operatorname{diag}(\boldsymbol{C}_{0,q}, \boldsymbol{C}_{1,q}, \ldots, \boldsymbol{C}_{N-1,q})\boldsymbol{Z}_{MN}^{Mq}. \quad (36)
\end{aligned}
$$

Finally, the right-hand side of (24) can be rewritten by using

$$
\begin{aligned}
&\left(\boldsymbol{F}_N \otimes \boldsymbol{I}_M\right)\left(\sum_{q=-Q}^{Q} \boldsymbol{H}'_q \boldsymbol{\Lambda}'_q\right)\left(\boldsymbol{F}_N^* \otimes \boldsymbol{I}_M\right) \\
&= \sum_{q=-Q}^{Q} \operatorname{diag}(\boldsymbol{C}_{0,q}, \boldsymbol{C}_{1,q}, \ldots, \boldsymbol{C}_{N-1,q})\boldsymbol{Z}_{MN}^{Mq}. \quad (37)
\end{aligned}
$$

As a result

$$
\begin{aligned}
&\boldsymbol{y}\boldsymbol{A}\left(\boldsymbol{F}_N^* \otimes \boldsymbol{I}_M\right) \\
&= \left(\boldsymbol{z}_{\mathrm{p},0\to Q}, \boldsymbol{z}_0 \boldsymbol{z}_1, \ldots, \boldsymbol{z}_{U-1}, \boldsymbol{z}_{\mathrm{p},-Q\to-1}\right) + \boldsymbol{\eta}' \\
&= \boldsymbol{x}_{\mathrm{m}} \sum_{q=-Q}^{Q} \operatorname{diag}(\boldsymbol{C}_{0,q}, \boldsymbol{C}_{1,q}, \ldots, \boldsymbol{C}_{N-1,q})\boldsymbol{Z}_{MN}^{Mq} + \boldsymbol{\eta}'
\end{aligned}
$$

$$(38)$$

and we can obtain (9) and (11) from (38) [the first M rows correspond to (9) and the remaining rows correspond to (11)], which is the left-hand side of (8). That concludes the proof.

APPENDIX B
PROOF OF (20) AND (21)

We would like to see more details of $\tilde{\boldsymbol{y}}$ in (14). At first, we focus on the right-hand side of (14), $\tilde{\boldsymbol{x}}$, where

$$
\begin{aligned}
\tilde{\boldsymbol{x}} &= \boldsymbol{x}_{\mathrm{m}}(\boldsymbol{F}_N \otimes \boldsymbol{I}_M, \boldsymbol{0}_{MN \times MN})\boldsymbol{F}_{2MN}^* \\
&= \boldsymbol{x}_{\mathrm{m}}\left(\hat{\boldsymbol{F}}_0, \hat{\boldsymbol{F}}_{2N}, \ldots, \hat{\boldsymbol{F}}_{2(M-1)N}\right). \quad (39)
\end{aligned}
$$

$$
(\boldsymbol{\Lambda}_{\mathrm{L},q}\boldsymbol{F}_N^* \otimes \boldsymbol{\Lambda}_{\mathrm{R},q}\boldsymbol{I}_M) = \begin{pmatrix}
W_N^0 \boldsymbol{\Lambda}_{\mathrm{R},q} & W_N^0 \boldsymbol{\Lambda}_{\mathrm{R},q} & \cdots & W_N^0 \boldsymbol{\Lambda}_{\mathrm{R},q} \\
W_N^q \boldsymbol{\Lambda}_{\mathrm{R},q} & W_N^{-1+q} \boldsymbol{\Lambda}_{\mathrm{R},q} & \cdots & W_N^{-N+q} \boldsymbol{\Lambda}_{\mathrm{R},q} \\
\vdots & \vdots & \ddots & \vdots \\
W_N^{(N-1)q} \boldsymbol{\Lambda}_{\mathrm{R},q} & W_N^{-(N-1)+(N-1)q} \boldsymbol{\Lambda}_{\mathrm{R},q} & \cdots & W_N^{-(N-1)^2+(N-1)q} \boldsymbol{\Lambda}_{\mathrm{R},q}
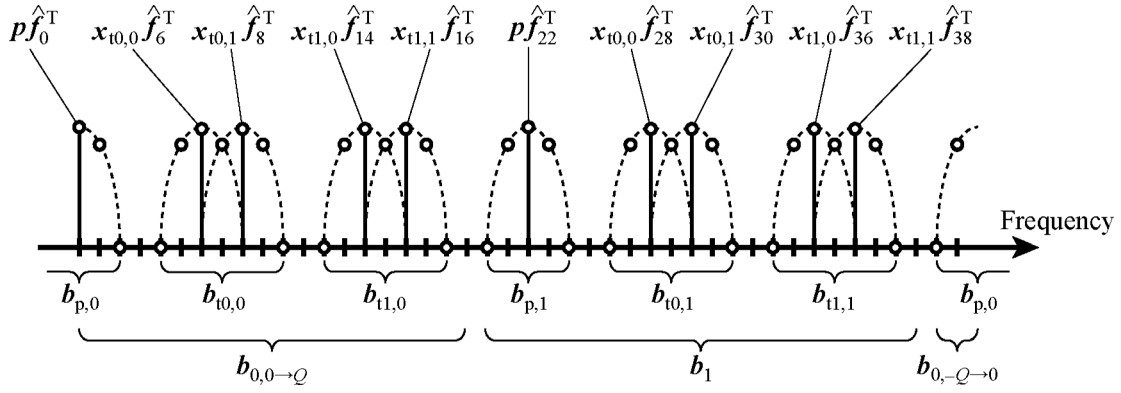\end{pmatrix}. \quad (35)
$$

Fig. 17.   Structure of $\tilde{\boldsymbol{x}}$ when $M = 2, P = 2, U = 2$, and $Q = 1$. Horizontal axes are discretized by $1/(2MNT)$.

$\hat{\boldsymbol{F}}_{2mN}$ is a matrix of size $MN \times 2N$ and (40), shown at the bottom of the page, where

$$c_{R,C} = \frac{1}{N}\left\{1 + \sqrt{-1}\tan\left[\frac{(-2R + C - N)\pi}{2N}\right]\right\}.$$

Note that we assume that the ICI beyond the direct subcarrier neighbors was neglected in (40). Now we can rewrite (39) as

$$\tilde{\boldsymbol{x}} = \boldsymbol{x}_{\mathrm{m}}(\boldsymbol{F}_N \otimes \boldsymbol{I}_M, \boldsymbol{0}_{MN \times MN})\boldsymbol{F}_{2MN}^* \qquad (41)$$

$$= (\boldsymbol{b}_{0,0 \to Q}, \boldsymbol{b}_1, \boldsymbol{b}_2, \ldots, \boldsymbol{b}_{M-1}, \boldsymbol{b}_{0,-Q \to -1}) \qquad (42)$$

where $\boldsymbol{b}_{0,-Q \to -1}$ and $\boldsymbol{b}_{0,0 \to Q}$ are vectors of length $2Q$ and $2(N - Q)$, respectively, and

$$\boldsymbol{b}_{0,-Q \to -1} = \left(\boldsymbol{0}_{1 \times (2Q-1)}, \boldsymbol{p}\hat{\boldsymbol{f}}_{2MN-1}^{\mathrm{T}}c_{0,2MN-1}\right) \qquad (43)$$

$$\boldsymbol{b}_{0,0 \to Q} = \left(\boldsymbol{p}\hat{\boldsymbol{f}}_0^{\mathrm{T}}, \boldsymbol{p}\hat{\boldsymbol{f}}_1^{\mathrm{T}}c_{0,1}, \boldsymbol{0}_{1 \times (2Q-1)}, 0,\right.$$
$$\left. \boldsymbol{b}_{\mathrm{t}0,0}, 0, \boldsymbol{b}_{\mathrm{t}1,0}, 0, \ldots, \boldsymbol{b}_{\mathrm{t}(U-1),0}, 0\right). \qquad (44)$$

$\boldsymbol{b}_m$ and $\boldsymbol{b}_{tu,m}$ are vectors of length $4Q + 1$ and $2P + 4Q - 1$, respectively, and

$$\boldsymbol{b}_{m'} = \left(\boldsymbol{b}_{\mathrm{p},m'}, 0, \boldsymbol{b}_{\mathrm{t}0,m'}, 0, \boldsymbol{b}_{\mathrm{t}1,m'}, 0, \ldots, \boldsymbol{b}_{\mathrm{t}(U-1),m'}, 0\right),$$
$$m' = 1, 2, \ldots, M-1 \qquad (45)$$

$$\boldsymbol{b}_{\mathrm{p},m'} = \left(\boldsymbol{0}_{1 \times (2Q-1)}, \boldsymbol{p}\hat{\boldsymbol{f}}_{2m'N-1}^{\mathrm{T}}c_{0,2m'N-1}, \boldsymbol{p}\hat{\boldsymbol{f}}_{2m'N}^{\mathrm{T}},\right.$$
$$\left. \boldsymbol{p}\hat{\boldsymbol{f}}_{2m'N+1}^{\mathrm{T}}c_{0,2m'N+1}, \boldsymbol{0}_{1 \times (2Q-1)}\right) \qquad (46)$$

$$\boldsymbol{b}_{tu,m} = \left(\boldsymbol{0}_{1 \times (2Q-1)}, \tilde{x}_{u,0,m}^{\mathrm{L}}, \tilde{x}_{u,0,m}, \tilde{x}_{u,0,m}^{\mathrm{R}} + \tilde{x}_{u,1,m}^{\mathrm{L}},\right.$$
$$\tilde{x}_{u,1,m}, \tilde{x}_{u,1,m}^{\mathrm{R}} + \tilde{x}_{u,2,m}^{\mathrm{L}}, \ldots, \tilde{x}_{u,1,P-2,m}^{\mathrm{R}}$$
$$\left. + \tilde{x}_{u,P-1,m}^{\mathrm{L}}, \tilde{x}_{u,P-1,m}, \tilde{x}_{u,P-1,m}^{\mathrm{R}}, \boldsymbol{0}_{1 \times (2Q-1)}\right) \qquad (47)$$

$$\tilde{x}_{u,p,m}^{\mathrm{L}} = \boldsymbol{x}_{tu,p}\hat{\boldsymbol{f}}_{g_N(u,p,m)-1}^{\mathrm{T}}c_{g(u,p),2g(u,p,m)-1}$$
$$\equiv \boldsymbol{x}_{tu,p}\hat{\boldsymbol{f}}_{g_N(u,p,m)}^{\mathrm{LT}} \qquad (48)$$

$$\tilde{x}_{u,p,m} = \boldsymbol{x}_{tu,p}\hat{\boldsymbol{f}}_{g_N(u,p,m)}^{\mathrm{T}} \qquad (49)$$

$$\tilde{x}_{u,p,m}^{\mathrm{R}} = \boldsymbol{x}_{tu,p}\hat{\boldsymbol{f}}_{g_N(u,p,m)+1}^{\mathrm{T}}c_{g(u,p),2g(u,p,m)+1}$$
$$\equiv \boldsymbol{x}_{tu,p}\hat{\boldsymbol{f}}_{g_N(u,p,m)}^{\mathrm{RT}} \qquad (50)$$

$$g(u,p) = 2Q + 1 + (P + 2Q)u + p$$
$$g_N(u,p,m) = 2mN + 2g(u,p).$$

Fig. 17 illustrates the relationship between $\tilde{\boldsymbol{x}}$ and $\boldsymbol{b}_{\mathrm{p},m}, \boldsymbol{b}_{tu,m}, \boldsymbol{b}_{0,-Q \to -1}, \boldsymbol{b}_{0,0 \to Q}$, and $\boldsymbol{b}_m$, when $M = 2, P = 2, U = 2$, and $Q = 1$. Now $\tilde{\boldsymbol{y}}$ can be expressed as

$$\tilde{\boldsymbol{y}} = \tilde{\boldsymbol{x}}\sum_{q=-Q}^{Q}\tilde{\boldsymbol{H}}_q\tilde{\boldsymbol{\Lambda}}_q + \tilde{\boldsymbol{\eta}},$$

$$= (\boldsymbol{b}_{0,0 \to Q}, \boldsymbol{b}_1, \boldsymbol{b}_2, \ldots, \boldsymbol{b}_{M-1}, \boldsymbol{b}_{0,-Q \to -1})$$

$$\times \sum_{q=-Q}^{Q}\tilde{\boldsymbol{H}}_q\tilde{\boldsymbol{\Lambda}}_q + \tilde{\boldsymbol{\eta}},$$

$$= (\boldsymbol{b}_{0,0 \to Q}^{\mathrm{r}}, \boldsymbol{b}_1^{\mathrm{r}}, \boldsymbol{b}_2^{\mathrm{r}}, \ldots, \boldsymbol{b}_{M-1}^{\mathrm{r}}, \boldsymbol{b}_{0,-Q \to -1}^{\mathrm{r}}) + \tilde{\boldsymbol{\eta}}. \qquad (51)$$

$\hat{\boldsymbol{F}}_{2mN}$

$$= \begin{pmatrix} \hat{\boldsymbol{f}}_{2mN}^{\mathrm{T}} & \hat{\boldsymbol{f}}_{2mN+1}^{\mathrm{T}}c_{0,2mN+1} & 0 & \hat{\boldsymbol{f}}_{2mN+3}^{\mathrm{T}}c_{0,2mN+3} & \cdots & 0 & \hat{\boldsymbol{f}}_{2N(m+1)-1}^{\mathrm{T}}c_{0,2N(m+1)-1} \\ 0 & \hat{\boldsymbol{f}}_{2mN+1}^{\mathrm{T}}c_{1,2mN+1} & \hat{\boldsymbol{f}}_{2mN+2}^{\mathrm{T}} & \hat{\boldsymbol{f}}_{2mN+3}^{\mathrm{T}}c_{1,2mN+3} & \cdots & 0 & \hat{\boldsymbol{f}}_{2N(m+1)-1}^{\mathrm{T}}c_{1,2N(m+1)-1} \\ \vdots & \vdots & \vdots & \vdots & \ddots & \vdots & \vdots \\ 0 & \hat{\boldsymbol{f}}_{2mN+1}^{\mathrm{T}}c_{N-1,2mN+1} & 0 & \hat{\boldsymbol{f}}_{2mN+3}^{\mathrm{T}}c_{N-1,2mN+3} & \cdots & \hat{\boldsymbol{f}}_{2\{N(m+1)-1\}}^{\mathrm{T}} & \hat{\boldsymbol{f}}_{2N(m+1)-1}^{\mathrm{T}}c_{N-1,2N(m+1)-1} \end{pmatrix}$$

$$\simeq \begin{pmatrix} \hat{\boldsymbol{f}}_{2mN}^{\mathrm{T}} & \hat{\boldsymbol{f}}_{2mN+1}^{\mathrm{T}}c_{0,2mN+1} & 0 & 0 & \cdots & 0 & \hat{\boldsymbol{f}}_{2N(m+1)-1}^{\mathrm{T}}c_{0,2N(m+1)-1} \\ 0 & \hat{\boldsymbol{f}}_{2mN+1}^{\mathrm{T}}c_{1,2mN+1} & \hat{\boldsymbol{f}}_{2mN+2}^{\mathrm{T}} & \hat{\boldsymbol{f}}_{2mN+3}^{\mathrm{T}}c_{1,2mN+3} & \cdots & 0 & 0 \\ \vdots & \vdots & \vdots & \vdots & \ddots & \vdots & \vdots \\ 0 & 0 & 0 & 0 & \cdots & \hat{\boldsymbol{f}}_{2\{N(m+1)-1\}}^{\mathrm{T}} & \hat{\boldsymbol{f}}_{2N(m+1)-1}^{\mathrm{T}}c_{N-1,2N(m+1)-1} \end{pmatrix}$$

$$(40)$$

We focus on specific subcarriers on $\tilde{y}$ corresponding to $\boldsymbol{b}_{\mathrm{p},m}$ and $\boldsymbol{b}_{\mathrm{t}u,m}$, and call them $\boldsymbol{b}_{\mathrm{p},m}^{\mathrm{r}}$ and $\boldsymbol{b}_{\mathrm{t}u,m}^{\mathrm{r}}$, respectively. In this case, $\boldsymbol{b}_{\mathrm{p},m}^{\mathrm{r}}$ can be expressed as

$$\boldsymbol{b}_{\mathrm{p},m}^{\mathrm{r}} = (\boldsymbol{h}_{-Q}, \boldsymbol{h}_{-Q+1}, \ldots, \boldsymbol{h}_{Q}) \boldsymbol{P}_m + \tilde{\boldsymbol{\eta}}_{\mathrm{p},m} \qquad (52)$$

where $\boldsymbol{P}_m$ is a matrix of size $M(2Q+1) \times (4Q+1)$, and we have (53), shown at the bottom of the page, and $\tilde{\boldsymbol{\eta}}_{\mathrm{p},m}$, is a sum of two noises: part of $\tilde{\boldsymbol{\eta}}$ and residual ICI. Moreover, $\boldsymbol{b}_{\mathrm{t}u,m}^{\mathrm{r}}$ can be expressed as

$$\boldsymbol{b}_{\mathrm{t}u,m}^{\mathrm{r}} = (\boldsymbol{h}_{-Q}, \boldsymbol{h}_{-Q+1}, \ldots, \boldsymbol{h}_{Q})$$

$$\times \begin{pmatrix} \check{\boldsymbol{X}}_{u,m} \boldsymbol{Z}_{2P+1}^{\mathrm{L}} & \boldsymbol{0}_{M \times (4Q-2)} & \\ \boldsymbol{0}_{M \times 1} & \check{\boldsymbol{X}}_{u,m} & \boldsymbol{0}_{M \times (4Q-3)} \\ \boldsymbol{0}_{M \times 3} & \check{\boldsymbol{X}}_{u,m} & \boldsymbol{0}_{M \times (4Q-5)} \\ & \vdots & \\ \boldsymbol{0}_{M \times (4Q-3)} & \check{\boldsymbol{X}}_{u,m} & \boldsymbol{0}_{M \times 1} \\ \boldsymbol{0}_{M \times (4Q-2)} & \check{\boldsymbol{X}}_{u,m} \boldsymbol{Z}_{2P+1}^{\mathrm{R}} & \end{pmatrix}$$

$$+ \tilde{\boldsymbol{\eta}}_{\mathrm{t}u,m} \qquad (54)$$

where $\boldsymbol{Z}_{2P+1}^{\mathrm{L}}$ and $\boldsymbol{Z}_{2P+1}^{\mathrm{R}}$ are matrices of size $(2P+1) \times (2P+1)$, and

$$\boldsymbol{Z}_{2P+1}^{\mathrm{L}} = \begin{pmatrix} 0 & 0 & \cdots & 0 & 0 \\ 1 & 0 & \cdots & 0 & 0 \\ 0 & 1 & \cdots & 0 & 0 \\ \vdots & \vdots & \ddots & \vdots & \vdots \\ 0 & 0 & \cdots & 1 & 0 \end{pmatrix}$$

$$\boldsymbol{Z}_{2P+1}^{\mathrm{R}} = \begin{pmatrix} 0 & 1 & 0 & \cdots & 0 \\ 0 & 0 & 1 & \cdots & 0 \\ \vdots & \vdots & \ddots & \vdots & \vdots \\ 0 & 0 & 0 & \cdots & 1 \\ 0 & 0 & 0 & \cdots & 0 \end{pmatrix} \qquad (55)$$

$$\check{\boldsymbol{X}}_{u,m} = \sum_{p=0}^{P-1} \Big[\Big(\hat{\boldsymbol{f}}_{g_N(u,p,m)-1}^{\mathrm{T}} \tilde{x}_{u,p,m}^{\mathrm{L}}, \hat{\boldsymbol{f}}_{g_N(u,p,m)}^{\mathrm{T}} \tilde{x}_{u,p,m}, $$
$$\hat{\boldsymbol{f}}_{g_N(u,p,m)+1}^{\mathrm{T}} \tilde{x}_{u,p,m}^{\mathrm{R}}, \boldsymbol{0}_{M \times (2P-2)} \Big) \boldsymbol{Z}_{2P+1}^{2p} \Big] \qquad (56)$$

and $\tilde{\boldsymbol{\eta}}_{\mathrm{t}u,m}$ is a sum of two noises: part of $\tilde{\boldsymbol{\eta}}$ and ICI. Now (54) can be reexpressed as

$$\boldsymbol{b}_{\mathrm{t}u,m}^{\mathrm{r}} = (\boldsymbol{x}_{\mathrm{t}u,0}, \boldsymbol{x}_{\mathrm{t}u,1}, \ldots, \boldsymbol{x}_{\mathrm{t}u,P-1}) \boldsymbol{H}_{u,m} + \tilde{\boldsymbol{\eta}}_{\mathrm{t}u,m} \qquad (57)$$

where $\boldsymbol{H}_{u,m}$ is a matrix of size $MP \times (2P+4Q-1)$, and we have (58) and (59), shown at the bottom of the page. By

$$\boldsymbol{P}_m = \begin{pmatrix} \hat{\boldsymbol{f}}_{2mN}^{\mathrm{T}} \boldsymbol{p} \hat{\boldsymbol{f}}_{2mN}^{\mathrm{T}} & \hat{\boldsymbol{f}}_{2mN+1}^{\mathrm{T}} \boldsymbol{p} \hat{\boldsymbol{f}}_{2mN+1}^{\mathrm{T}} c_{0,2mN+1} & 0 & 0 & \cdots \\ 0 & \hat{\boldsymbol{f}}_{2mN-1}^{\mathrm{T}} \boldsymbol{p} \hat{\boldsymbol{f}}_{2mN-1}^{\mathrm{T}} c_{0,2mN-1} & \hat{\boldsymbol{f}}_{2mN}^{\mathrm{T}} \boldsymbol{p} \hat{\boldsymbol{f}}_{2mN}^{\mathrm{T}} & \hat{\boldsymbol{f}}_{2mN+1}^{\mathrm{T}} \boldsymbol{p} \hat{\boldsymbol{f}}_{2mN+1}^{\mathrm{T}} c_{0,2mN+1} & \cdots \\ \vdots & \vdots & \vdots & \vdots & \ddots \\ 0 & 0 & 0 & 0 & \cdots \\ 0 & 0 & 0 & 0 & \cdots \\ & \cdots & 0 & 0 & 0 \\ & \cdots & 0 & 0 & 0 \\ & \ddots & \vdots & \vdots & \vdots \\ & \cdots & \hat{\boldsymbol{f}}_{2mN+1}^{\mathrm{T}} \boldsymbol{p} \hat{\boldsymbol{f}}_{2mN+1}^{\mathrm{T}} c_{0,2mN+1} & 0 & 0 \\ & \cdots & \hat{\boldsymbol{f}}_{2mN-1}^{\mathrm{T}} \boldsymbol{p} \hat{\boldsymbol{f}}_{2mN-1}^{\mathrm{T}} c_{0,2mN-1} & \hat{\boldsymbol{f}}_{2mN}^{\mathrm{T}} \boldsymbol{p} \hat{\boldsymbol{f}}_{2mN}^{\mathrm{T}} & \hat{\boldsymbol{f}}_{2mN+1}^{\mathrm{T}} \boldsymbol{p} \hat{\boldsymbol{f}}_{2mN+1}^{\mathrm{T}} c_{0,2mN+1} \end{pmatrix} \qquad (53)$$

$$\boldsymbol{H}_{u,m} = \left(\check{\boldsymbol{H}}_{-Q,u,m} \boldsymbol{Z}_{2P+1}^{\mathrm{L}}, \boldsymbol{0}_{M \times (4Q-2)} \right) + \sum_{q=-Q+1}^{Q-1} \left(\boldsymbol{0}_{M \times \{2(Q+q)-1\}}, \check{\boldsymbol{H}}_{q,u,m}, \boldsymbol{0}_{M \times \{2(Q-q)-1\}} \right)$$
$$+ \left(\boldsymbol{0}_{M \times (4Q-2)}, \check{\boldsymbol{H}}_{Q,u,m} \boldsymbol{Z}_{2P+1}^{\mathrm{R}} \right) \qquad (58)$$

and

$$\check{\boldsymbol{H}}_{q,u,m} = \begin{pmatrix} \tilde{\boldsymbol{h}}_{q,u,0,m}^{\mathrm{LT}} & \tilde{\boldsymbol{h}}_{q,u,0,m}^{\mathrm{T}} & \tilde{\boldsymbol{h}}_{q,u,0,m}^{\mathrm{RT}} & 0 & \cdots & 0 & 0 & 0 \\ 0 & 0 & \tilde{\boldsymbol{h}}_{q,u,1,m}^{\mathrm{LT}} & \tilde{\boldsymbol{h}}_{q,u,1,m}^{\mathrm{T}} & \cdots & 0 & 0 & 0 \\ \vdots & \vdots & \vdots & \vdots & \ddots & \vdots & \vdots & \vdots \\ 0 & 0 & 0 & 0 & \cdots & \tilde{\boldsymbol{h}}_{q,u,P-2,m}^{\mathrm{RT}} & 0 & 0 \\ 0 & 0 & 0 & 0 & \cdots & \tilde{\boldsymbol{h}}_{q,u,P-1,m}^{\mathrm{LT}} & \tilde{\boldsymbol{h}}_{q,u,P-1,m}^{\mathrm{T}} & \tilde{\boldsymbol{h}}_{q,u,P-1,m}^{\mathrm{RT}} \end{pmatrix} \qquad (59)$$

$$\tilde{\boldsymbol{h}}_{q,u,p,m}^{\mathrm{LT}} = \hat{\boldsymbol{f}}_{g_N(u,p,m)}^{\mathrm{LT}} \boldsymbol{h}_q \hat{\boldsymbol{f}}_{g_N(u,p,m)-1}^{\mathrm{T}}$$
$$\tilde{\boldsymbol{h}}_{q,u,p,m}^{\mathrm{T}} = \hat{\boldsymbol{f}}_{g_N(u,p,m)}^{\mathrm{T}} \boldsymbol{h}_q \hat{\boldsymbol{f}}_{g_N(u,p,m)}^{\mathrm{T}}$$
$$\tilde{\boldsymbol{h}}_{q,u,p,m}^{\mathrm{RT}} = \hat{\boldsymbol{f}}_{g_N(u,p,m)}^{\mathrm{RT}} \boldsymbol{h}_q \hat{\boldsymbol{f}}_{g_N(u,p,m)+1}^{\mathrm{T}} \cdot$$

combining (52) for all m, we can obtain (20) as

$$
\begin{aligned}
&\left(\boldsymbol{b}_{\mathrm{p},0}^{\mathrm{r}}, \boldsymbol{b}_{\mathrm{p},1}^{\mathrm{r}}, \ldots, \boldsymbol{b}_{\mathrm{p},M-1}^{\mathrm{r}}\right) \\
&= \left(\boldsymbol{h}_{-Q}, \boldsymbol{h}_{-Q+1}, \ldots, \boldsymbol{h}_{Q}\right)\left(\boldsymbol{P}_0, \boldsymbol{P}_1, \ldots, \boldsymbol{P}_{M-1}\right) \\
&\quad + \left(\tilde{\boldsymbol{\eta}}_{\mathrm{p}0}, \tilde{\boldsymbol{\eta}}_{\mathrm{p}1}, \ldots, \tilde{\boldsymbol{\eta}}_{\mathrm{p}M-1}\right) \\
&\Rightarrow \boldsymbol{b}_{\mathrm{pc}}^{\mathrm{r}} = \left(\boldsymbol{h}_{-Q}, \boldsymbol{h}_{-Q+1}, \ldots, \boldsymbol{h}_{Q}\right)\boldsymbol{P}_{\mathrm{c}} + \tilde{\boldsymbol{\eta}}_{\mathrm{pc}}.
\end{aligned}
$$

Moreover, by combining (57) for all m, we can obtain (21) as

$$
\begin{aligned}
&\left(\boldsymbol{b}_{tu,0}^{\mathrm{r}}, \boldsymbol{b}_{tu,1}^{\mathrm{r}}, \ldots, \boldsymbol{b}_{tu,M-1}^{\mathrm{r}}\right) \\
&= \left(\boldsymbol{x}_{tu,0}, \boldsymbol{x}_{tu,1}, \ldots, \boldsymbol{x}_{tu,P-1}\right)\left(\boldsymbol{H}_{u,0}, \boldsymbol{H}_{u,1}, \ldots, \boldsymbol{H}_{u,M-1}\right) \\
&\quad + \left(\tilde{\boldsymbol{\eta}}_{tu,0}, \tilde{\boldsymbol{\eta}}_{tu,1}, \ldots, \tilde{\boldsymbol{\eta}}_{tu,M-1}\right) \\
&\Rightarrow \boldsymbol{b}_{tcu}^{\mathrm{r}} = \boldsymbol{x}_{tu}\boldsymbol{H}_{cu} + \tilde{\boldsymbol{\eta}}_{tcu}.
\end{aligned}
$$

That concludes the proof.

ACKNOWLEDGMENT

REFERENCES

[1] T. B. Curtin, J. G. Bellingham, J. Catipovic, and D. Webb, "Autonomous oceanographic sampling networks," *Oceanography*, vol. 6, no. 3, pp. 86–94, 1993.
[2] J. Catipovic, D. Brady, and S. Etchemendy, "Development of underwater acoustic modems and networks," *Oceanography*, vol. 6, no. 3, pp. 112–119, 1993.
[3] E. M. Sozer, M. Stojanovic, and J. G. Proakis, "Underwater acoustic networks," *IEEE J. Ocean. Eng.*, vol. 25, no. 1, pp. 72–83, Jan. 2000.
[4] I. F. Akyildiz, D. Pompili, and T. Melodia, "Underwater acoustic sensor networks: Research challenges," *Ad Hoc Netw.*, vol. 3, pp. 257–279, 2005.
[5] J. Heidemann, W. Ye, J. Wills, A. Syed, and Y. Li, "Research challenges and applications for underwater sensor networking," in *Proc. Wireless Commun. Netw. Conf.*, 2006, pp. 228–235.
[6] J. Heidemann, M. Stojanovic, and M. Zorzi, "Underwater sensor networks: Applications, advances and challenges," *Philosoph. Trans. Roy. Soc. A*, vol. 370, pp. 158–175, 2011.
[7] H. Ochi, T. Tsuchiya, Y. Amitani, M. Suzuki, and S. Negishi, "Study on color video pictures transmission by digital acoustic signal," in *Proc. Conf. Pacific Ocean Environ. Probing*, 1992, pp. 132–137.
[8] M. Stojanovic, J. Catipovic, and J. Proakis, "Phase coherent digital communications for underwater acoustic channels," *IEEE J. Ocean. Eng.*, vol. 19, no. 1, pp. 100–111, Jan. 1994.
[9] T. H. Eggen, A. B. Baggeroer, and J. C. Preisig, "Communication over Doppler spread channels—Part I: Channel and receiver presentation," *IEEE J. Ocean. Eng.*, vol. 25, no. 1, pp. 62–71, Jan. 2000.
[10] T. H. Eggen, J. C. Preisig, and A. B. Baggeroer, "Communication over Doppler spread channels—Part II: Receiver characterization and practical results," *IEEE J. Ocean. Eng.*, vol. 26, no. 4, pp. 612–621, Oct. 2001.
[11] E. M. Sozer, J. G. Proakis, and F. Clackmon, "Iterative equalization and decoding techniques for shallow water acoustic channels," in *Proc. OCEANS Conf.*, 2001, vol. 4, pp. 2201–2208.
[12] S. Coatelan and A. Glavieux, "Design and test of a coding OFDM system on the shallow water acoustic channel," in *Proc. OCEANS Conf.*, 1995, vol. 3, pp. 2065–2070.
[13] M. Stojanovic, "Low complexity OFDM detector for underwater acoustic channel," in *Proc. OCEANS Conf.*, 2006, DOI: 10.1109/OCEANS.2006.307057.
[14] B. Li, S. Zhou, M. Stojanovic, L. Freitag, and P. Willett, "Multicarrier communication over underwater acoustic channels with nonuniform Doppler shifts," *IEEE J. Ocean. Eng.*, vol. 33, no. 2, pp. 198–209, Apr. 2008.
[15] F. Qu and L. Yang, "Basis expansion model for underwater acoustic channels?," in *Proc. OCEANS Conf.*, 2008, DOI: 10.1109/OCEANS.2008.5151896.
[16] G. Leus and P. A. Walree, "Multiband OFDM for covert acoustic communications," *IEEE J. Sel. Areas Commun.*, vol. 26, no. 9, pp. 1662–1673, Dec. 2008.
[17] S. J. Hwang and P. Schniter, "Efficient multicarrier communication for highly spread underwater acoustic channels," *IEEE J. Sel. Areas Commun.*, vol. 26, no. 9, pp. 1674–1683, Dec. 2008.
[18] S. F. Mason *et al.*, "Receiver comparisons on an OFDM design for Doppler spread channels," in *Proc. OCEANS Conf.*, 2009, DOI: 10.1109/OCEANSE.2009.5278224.
[19] Z. Wang, S. Zhou, G. B. Giannakis, C. R. Berger, and J. Huang, "Frequency-domain oversampling for zero-padded OFDM in underwater acoustic communications," *IEEE J. Ocean. Eng.*, vol. 37, no. 1, pp. 14–24, Jan. 2012.
[20] Y. M. Aval and M. Stojanovic, "Differentially coherent multichannel detection of acoustic OFDM signals," *IEEE J. Ocean. Eng.*, vol. 40, no. 2, pp. 251–268, Apr. 2015.
[21] N. Suehiro, C. Han, T. Imoto, and N. Kuroyanagi, "An information transmission method using Kronecker product," in *Proc. IASTED Int. Conf. Commun. Syst. Netw.*, 2002, pp. 206–209.
[22] N. Suehiro, C. Han, and T. Imoto, "Very efficient wireless frequency usage based on pseudo-coherent addition of multipath signals using Kronecker product with rows of DFT matrix," in *Proc. Int. Symp. Inf. Theory*, 2003, DOI: 10.1109/ISIT.2003.1228401.
[23] N. Suehiro, R. Jin, C. Han, and T. Hashimoto, "Performance of very efficient wireless frequency usage system using Kronecker product with rows of DFT matrix," in *Proc. IEEE Inf. Theory Workshop*, 2006, pp. 526–529.
[24] T. Ebihara and N. Suehiro, "The orthogonal signal division multiplexing and its performance evaluation," (in Japanese) *IEICE Trans.*, vol. J91-B, pp. 1086–1094, 2008.
[25] S. Zhou, G. B. Giannakis, and C. L. Martret, "Chip-interleaved block-spread code division multiple access," *IEEE Trans. Commun.*, vol. 50, no. 2, pp. 235–248, Feb. 2002.
[26] T. Ebihara and K. Mizutani, "Underwater acoustic communication with an orthogonal signal division multiplexing scheme in doubly spread channels," *IEEE J. Ocean. Eng.*, vol. 39, no. 1, pp. 47–58, Jan. 2014.
[27] G. Leus, S. Zhou, and G. B. Giannakis, "Orthogonal multiple access over time- and frequency-selective channels," *IEEE Trans. Inf. Theory*, vol. 49, no. 8, pp. 1942–1950, Aug. 2003.
[28] A. M. Sayeed and B. Aazhang, "Joint multipath-Doppler diversity in mobile wireless communications," *IEEE Trans. Commun.*, vol. 47, no. 1, pp. 123–132, Jan. 1999.
[29] T. Zemen and C. F. Mecklenbrauker, "Time-variant channel estimation using discrete prolate spheroidal sequences," *IEEE Trans. Signal Process.*, vol. 53, no. 9, pp. 3597–3607, Sep. 2005.

Tadashi Ebihara (S'09–M'10) was born in Tokyo, Japan, in 1986. He received the Ph.D. degree from the University of Tsukuba, Tsukuba, Japan, in 2010.

He received the Research Fellowship for Young Scientists (DC1), Japan Society for the Promotion of Science (JSPS), 2009–2010. From September 2013 until December 2013 he was a Visiting Professor at the Delft University of Technology, Delft, The Netherlands. He is currently an Assistant Professor at the Faculty of Engineering, Information and Systems, University of Tsukuba. His research interests include mobile communications and their applications to underwater acoustic communication systems.

Geert Leus (M'01–SM'05–F'12) was born in Leuven, Belgium, in 1973. He received the Electrical Engineering degree and the Ph.D. degree in applied sciences from the Katholieke Universiteit Leuven, Leuven, Belgium, in June 1996 and May 2000, respectively.

He was a Research Assistant and a Postdoctoral Fellow of the Fund for Scientific Research, Flanders, Belgium, from October 1996 until September 2003. During that period, he was affiliated with the Electrical Engineering Department, Katholieke Universiteit Leuven. Currently, he is a Professor with the Faculty of Electrical Engineering, Mathematics and Computer Science, Delft University of Technology, Delft, The Netherlands. During summer 1998, he visited Stanford University, Stanford, CA, USA, and from March 2001 until May 2002, he was a Visiting Researcher and Lecturer at the University of Minnesota, Minneapolis, MN, USA. His research interests are in the area of signal processing for communications.

Dr. Leus received the 2002 IEEE Signal Processing Society Young Author Best Paper Award and the 2005 IEEE Signal Processing Society Best Paper Award.